Title: Luminescence properties of tetrahedral coordinated Mn2+ : genthelvite and willemite examples

Author: Maria Czaja, Radosław Lisiecki, Rafał Juroszek, Tomasz Krzykawski

Citation style: Czaja Maria, Lisiecki Radosław, Juroszek Rafał, Krzykawski Tomasz. (2021). Luminescence properties of tetrahedral coordinated Mn2+ : genthelvite and willemite examples. „Minerals (Basel)" (Vol. 11, iss. 11, 2021, art. no. 1215, s. 1-27), DOI:10.3390/min11111215

minerals

MDPI

Article

Luminescence Properties of Tetrahedral Coordinated Mn^{2+}; Genthelvite and Willemite Examples

Maria Czaja [1,*], Radosław Lisiecki [2], Rafał Juroszek [1] and Tomasz Krzykawski [2]

[1] Institute of Earth Sciences, Faculty of Natural Science, University of Silesia, Będzińska 60, 41-200 Sosnowiec, Poland; rafal.juroszek@us.edu.pl
[2] Institute of Low Temperature and Structure Research, Polish Academy of Sciences, Okólna 2, 50-422 Wrocław, Poland; r.lisiecki@intibs.pl (R.L.); tomasz.krzykawski@us.edu.pl (T.K.)
* Correspondence: maria.czaja@us.edu.pl

Abstract: The cause of the split of $^4A^4E(^4G)$ Mn^{2+} excited level measured on minerals spectra is discussed. It is our view that $\Delta E = |4E(4G) - 4A(4G)|$ should be considered an important spectroscopic parameter. Among the possible reasons for the energy levels splitting taken under consideration, such as the covalent bond theory, the geometric deformation of the coordination polyhedron and the lattice site's symmetry, the first one was found to be inappropriate. Two studied willemite samples showed that the impurities occur in one of the two available lattice sites differently in both crystals. Moreover, it was revealed that the calculated crystal field *Dq* parameter can indicate which of the two non-equivalent lattice sites positions in the willemite crystal structure was occupied by Mn^{2+}. The above conclusions were confirmed by X-ray structure measurements. Significant differences were also noted in the Raman spectra of these willemites.

Keywords: Mn^{2+}; luminescence; energy of excited level; crystal field parameters

Citation: Czaja, M.; Lisiecki, R.; Juroszek, R.; Krzykawski, T. Luminescence Properties of Tetrahedral Coordinated Mn^{2+}; Genthelvite and Willemite Examples. *Minerals* **2021**, *11*, 1215. https://doi.org/10.3390/min11111215

Academic Editors: Gioacchino Tempesta and Giovanna Agrosì

Received: 3 October 2021
Accepted: 25 October 2021
Published: 30 October 2021

1. Introduction

The luminescence of synthetic materials subsidized with manganese ions, especially (2+), is still intensively researched and has been for many years [1,2]. The emission color of subsidized Mn^{2+} compounds is usually green or orange to red. It depends on the strength of the crystal field, i.e., the coordination number, the type of ligand and the distance between the ligand and the manganese ion. Various materials with a halides, oxides, phosphates and silicate matrix are synthesized in the form of glass, ceramics, and crystals, sometimes as nanomaterials or coatings. Many synthetic materials are doped not only with Mn^{2+} but also with lanthanide ions. Then, between the Mn^{2+} and $4f^n$ ions, the phenomenon of energy transfer takes place [3]. This makes it possible to obtain efficient light emitters of various colors, including white light. Moreover, some of these materials exhibit a persistent luminescence phenomenon [4,5].

It is believed that the study of the spectroscopic properties of natural materials containing Mn^{2+} could be inspiring to create an optical material with the desired parameters. Divalent manganese ion is one of the most common and well-known activators of minerals' luminescence.

The present research has demonstrated some properties of the luminescence spectra of Mn^{2+}-bearing minerals. First, attention was paid to the splitting of the $^4E^4A(^4G)$ excited level. The absorption/excitation bands corresponded to Mn^{2+} transitions were usually measured in the 300–580 nm range and these bands sometimes have not been single. On these spectra, the υ_3 band of $^6S \rightarrow {}^4E^4A_1(^4G)$ transition is usually distinguished due to its intensity and sharpness. It was also often measured, but not clarified, that this band is double. A review of available absorption/excitation spectra for Mn^{2+}-bearing minerals and synthetic materials concludes that $\Delta E = |{}^4E(^4G) - {}^4A(^4G)|$, i.e., splitting of these levels is an important spectroscopic parameter. In the current article, an attempt to

indicate the factors affecting the ΔE value for two minerals that contain Mn^{2+} in tetrahedral coordination: genthelvite $Be_3Zn_4(SiO_4)_3S$ and willemite Zn_2SiO_4 was made.

For all minerals and an overwhelming number of synthetic phosphors, Mn^{2+} occurring as a high-spin complex possessing the unique electronic configuration $(t_{2g})^3(e_g)^2$ with a single occupation of all five d orbitals and Crystal Field Stabilization Energy (*CSFE*) equal to zero [6]. As a consequence, Mn^{2+} can be equally likely present in both octahedral and tetrahedral coordination. Tanabe–Sugano diagram for d^5 ion is presented in Figure 1a. The ground term is ^6S and the ground level is $^6A_1$ with the five 5d electrons orbitals (t_{2g} ↑)^3(e_g ↑)^2. In order of increasing energy, the excited terms are: ^4G, ^4P, ^4D, ^1I and ^4F. Due to the crystal field, the terms split into levels. For example, the first excited term ^4G splits into levels $^4T_{2g}$ and $^4T_{1g}$, whose energy strongly depends on crystal field parameter *Dq* and two levels $^4A_1$ and ^4E_g, which are independent on *Dq*. For an ion in tetrahedral coordination, the letter "g" in the subscript is not written. Figure 1b shows the electron configuration of the ground level and some of the excited crystal field levels of d^5 ion in tetrahedral coordination.

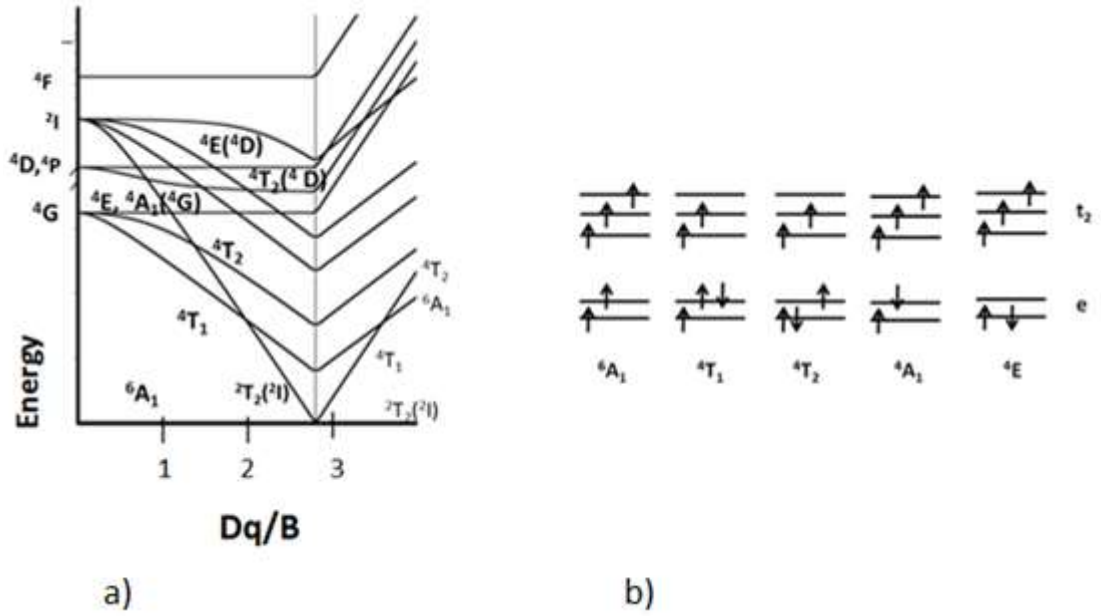

Figure 1. The energy levels of d^5 ion: (**a**) simplified Tanabe–Sugano diagram (sketched after [7]); (**b**) electronic configuration of d^5 ion, high spin (HS) and tetrahedral coordination.

The transitions between ground and excited states according to the solution of the Tanabe–Sugano theory are as expressed in Equation (1). In the visible region, there are five transitions measured as υ_1–υ_5 bands listed below in the order of increasing energy:

$$\begin{gathered} \vartheta_1 : {}^6A_1(S) \rightarrow {}^4T_{1g}({}^4G) = -10Dq + 10B + 6C - 26\tfrac{B^2}{10Dq}, \\ \vartheta_2 : {}^6A_1(S) \rightarrow {}^4T_{2g}({}^4G) = -10Dq + 18B + 6C - 38\tfrac{B^2}{10Dq}, \\ \vartheta_3 : {}^6A_1(S) \rightarrow {}^4E_g, {}^4A_{1g}({}^4G) = 10B + 5C, \\ \vartheta_4 : {}^6A_1(S) \rightarrow {}^4T_{2g}({}^4D) = 13B + 5C + x, \\ \vartheta_5 : {}^6A_1(S) \rightarrow {}^4E_g({}^4D) = 17B + 5C, \end{gathered} \quad (1)$$

where *B* and *C* are the Racah parameters. From these equations, the *B*, *C* and *Dq* parameters could be calculated. Usually, the *B* parameter is calculated first, from the difference among υ_5 and υ_3 bands. However, if the υ_3 and/or υ_5 band is not a single band, but rather a split one, determining the values of parameters *B* and *C* becomes problematic. The *Dq*

parameter is calculated from υ_2 or υ_1 transition, the band which is better distinguished in the spectrum. Then Equations (2) or (3) are used:

$$100Dq^2 = (14B + 5C - E(\vartheta_2)(22B + 7C - E(\vartheta_2) + 12B^2\frac{(E(\vartheta_2) - 22B - 7C)}{(13B + 5C - E(\vartheta_2)} \quad (2)$$

$$100Dq^2 = (10B + 7C - E(\vartheta_1)(10B + 5C - E(\vartheta_1) + 36B^2\frac{(E(\vartheta_1) - 10B - 5C)}{(19B + 7C - E(\vartheta_1)} \quad (3)$$

The $^4E^4A_1$ level is the efficient level for the excitation of the emission of the Mn^{2+}. Therefore, it has been concluded that the previously known theories explaining the causes of this level splitting should be considered. In general, the reasons of the complex nature of absorption/excitation band may be as follows:

(a) The excited states have a mixed nature; for example, the ^4G level is influenced by ^4D or ^4P levels. The $^4A_{1g}(^4G)$ level is expected to be less affected than the $^4E_g(^4G)$ level by slight changes in the metal-ligand distances. The mixed nature of the excited states was assumed for Mn^{2+} site in apatite [8] and then the non-zero ΔE was calculated. However, this assumption was not made in the current study.

(b) The electron d-d transitions are strongly coupled with lattice vibrations, so the υ_1 and υ_2 transitions would not be single only at room temperature and the emission band should become narrower at low temperatures. However, it was sometimes difficult to unequivocally prove whether the measured υ_1 and υ_2 bands were single or complex. Accordingly, this effect could not be recognized as an important factor for ΔE value.

(c) Mn^{2+} occupies more than one inequivalent crystal site. If the Mn^{2+} with the same or similar quantities occupies two sites with different Dq values, the υ_1, υ_2 and υ_4 transitions would not be single. Such effect should be observed not only at low temperature but also at room temperature. This case was found for T1 and T2 sites of willemite by Halenius et al. [9]. Despite the significant difference of υ_1, υ_2 and Dq values for these sites, Halenius et al. [9] did not mention whether the emission band was double or not. In addition, the same B and C parameters were assigned for T1 and T2 sites [9]. According to [9], the difference of occupied sites does not imply a difference in the nature of the bond. Such a case is discussed in Section 3.5.

(d) In this work, we have also verified whether the ΔE value depends on the geometrical deformation of coordination polyhedron. For each lattice site which Mn^{2+} can occupy, the following parameters were calculated: quadratic elongation (l), bond angle variance ($s_q{}^2$), distortion index (s) [10] and mean quadratic elongation Δ [11] defined for coordination CN = 4 as $< l(CN = 4) > \frac{1}{4}\sum_{i=1}^{4}\left(\frac{l_i}{l_0}\right)^2$, $\sigma^2_{\theta(tetr)} = \sum_{i=1}^{6}\left(\frac{\theta_i - 109.47^\circ}{5}\right)$, $\sigma(CN = 4) = \sqrt[2]{\frac{1}{4}\sum_{i-1}^{4}(l_i - l_0)^2}$ and $\Delta = \frac{1}{4}\sum_{i=1}^{4}\left(\frac{l_i - l_0}{l_0}\right)^2$. The l_i is individual Me-O bond length, l_0 is the main bond length for each site, and the θ_i is individual O-Me-O angle. The emission band could be a single band for each site. These deformation parameters are discussed in Section 3.5.

(e) The contribution of covalence participation in Mn-ligand bonding. The degeneracy of states $^4E(^4G)$ and $^4A_1(^4G)$ could be lifted by covalence in the crystal. The removal of degeneracy can be explained by the differential expansion of (t_{2g}) and (e_g) orbitals due to differing covalence between t_2 and e orbitals. Curie et al. [12] and Stout [13] proposed to introduce parameters taking into account the participation of the covalent bond. These are: the Koide–Pryce parameter ε, the Racah–Trees parameter α, and finally, the N_t and N_e normalization parameters. The values of the Racah B and C parameters as well as the energy values of the energy levels change (Equation (4)):

$$\begin{gathered}\vartheta_1 : -10Dq + 10B + 6C - \frac{26B^2}{10Dq} + 22\alpha,\ \vartheta_2 : -10Dq + 18B + 6C - \frac{38B^2}{10Dq} + 26\alpha,\ \vartheta_3 : 10B + 5C + 20\alpha \\ \vartheta_4 : 13B + 5C + 8\alpha,\ \vartheta_5 : 17B + 5C + 6\alpha,\ B = \frac{94\alpha \pm \sqrt{49(\vartheta_5 - \vartheta_3)^2 - 768\alpha^2}}{49},\ C = \frac{\vartheta_5 + \vartheta_3 - 27B - 26\alpha}{10}\end{gathered} \quad (4)$$

For octahedral coordination $N_t = 1$, $N_e^2 = 1 - \varepsilon$, for tetrahedral coordination $N_e = 1$, $N_t^2 = 1 - \varepsilon$. As a consequence of the covalent bond, the B' and C' Racah parameters are smaller than for free ion B and C and equal: for tetrahedral coordination $B' = BN_e^4$, $C' = CN_e^4$, $\varepsilon = 1 - \frac{N_t^2}{N_e^2}$, and $B' = BN_t^4$, $C' = CN_t^4$, $\varepsilon = 1 - \frac{N_e^2}{N_t^2}$ for octahedral coordination. According to [12] $^6A_1(^6S) \rightarrow {}^4A_1(^4G) = (10B + 5C)N_t^2N_e^2$ $^4E(^4G, {}^4D) \rightarrow {}^6A_1(^6S)$ are the eigenvalues of the matrix

$$\begin{bmatrix} (9B + 5C)N_t^4 + (4B + 2C)N_t^2N_e^2 & 2\sqrt{3}BN_t^2N_e^2 \\ 2\sqrt{3}BN_t^2N_e^2 & (6B + 3C)N_t^2N_e^2 + (8B + 2C)N_e^4 \end{bmatrix} \quad (5)$$

Section 3.5 shows the result of the calculations made in accordance with the Equations (4) and (5).

(f) The crystal site of Mn^{2+} has effective low symmetry. As the site symmetry is reduced from octahedral, cubic, or tetrahedral to C_1, C_s, C_i, C_2, C_{2v}, C_{2h}, D_2 and D_{2h}, the double (E) or triple (T) orbital degeneracy is removed or reduced. Palumbo and Brown [14] measured several excitation spectra of Mn-bearing crystals. The splitting of almost all Mn^{2+} excited levels was measured at low temperature in several crystals, such as ZnF_2, ZnS, Zn_3PO_4, chlor-and fluor- Cd phosphates, Zn_2SiO_4 willemite, and Zn-spinel. After [14], the excitation of $^4E^4A(^4G)$ level exhibits 3 lines, for Zn_2SiO_4: 0.06 Mn with ΔE = 147 cm^{-1}. Calculation of the energy of excited levels whose orbital degeneracy has been removed due to low symmetry of occupied site or coordination polyhedron is presented as a solution of the following crystal field Hamiltonian $H = \sum_{p=2}, \sum_{4k=-p}^{p} B_p^k \cdot O_p^k$ [15,16]. Energy values of the excited levels, without imaginary terms, can be obtained for a symmetry of position not lower than orthorhombic. In other cases, the approximation of the orthorhombic field is used. Such calculations are successfully performed for $4f^n$ ions. Brik et al. [17] for $LiAlO_2$:Mn^{2+} (0.034 at%) and C_2 symmetry measured that ΔE = 616 cm^{-1}, while calculated only ΔE = 428 cm^{-1}. For Mn^{2+} in willemite, Vaida [18,19] showed two sets of $B_p{}^k$ parameters and calculated energy levels. These data are presented in Table 7. In the previous one [18], splitting energy levels was neither observed nor calculated, contrary to Su et al. [20]. While the proper value of B (622 cm^{-1}), C (3504 cm^{-1}), and Dq (562 cm^{-1}) parameters have been obtained. In the second [19], with changed B_p^k parameters, a complete split of energy levels was observed, but the obtained values of parameters B (945 cm^{-1}), C (2851 cm^{-1}), and Dq (340.5 cm^{-1}) are rather not credible. Both of the above examples [17–19] showed that this method of calculation energy of excited levels of Mn^{2+} present in a low symmetrical lattice site does not give results consistent with the experimental data. Due to the low symmetry of the lattice site and the insufficient amount of experimental input data, especially the position of the υ_1 band, no such calculations were made for the minerals studied in this work.

In this article, we present a discussion of the influence of the following factors on the value of ΔE, i.e., ($^4E^4A_1(^4G)$) splitting—geometric deformation of lattice site, participation of covalent bond and, only qualitatively, a low position symmetry. We also discuss the possibility of Mn^{2+} being present in two non-equivalent lattice sites in willemite samples.

2. Materials and Methods

All studied here minerals showed an intense green luminescence (Figure 2).

Two specimens of genthelvite $Be_3Zn_4(SiO_4)_3S$ from Poudrette quarry Mont Saint-Hilaire (Quebec, QC, Canada) have been studied in the current research. They have light yellow (G1) or yellow (G2) color and are tristetrahedrons, most probably tetrahedrally-shaped {112} and {114} (Figure 2, photo 1a, b). These crystals' sizes are relatively small, up to 2.5 mm. Genthelvite belongs to tectosilicates and may be considered as a member of the sodalite $Na_4(Si_3Al_3)O_{12}Cl$ subgroup, where Be is playing the role of Al. The crystal structure of genthelvite was resolved by Hassan and Grundy [21]. Crystal space group is $P\bar{4}3n$, number of formula unit Z = 2, the lattice unit recognized as a standard a = 8.1091(4) Å for the sample with minimal Mn-content 0.95 wt.%. The SiO_4 and BeO_4 polyhedrons are

linked and make up the cages with central sulphur, the common apex for two ZnO_3S tetrahedra. It is believed [22] that Mn substitutes for Zn in ZnO_6S trigonal pyramid, coordination number CN = 7, with three Zn-O bond lengths 1.9481 Å, three other 3.1076 Å and one Zn-S equal 2.3628 Å. However, it is most often assumed that Zn has the subsequent four ligands O_3S, with a mean Zn-ligand distance equal to 2.0615 Å, but an effective coordination number of Zn is equal to 3.3608 [21]. Wyckoff's position of all atoms in genthelvite structure is 8e, the site symmetry of Zn atoms is rather high—C_3. The sketch of the genthelvite crystal structure is presented in Figure 3a.

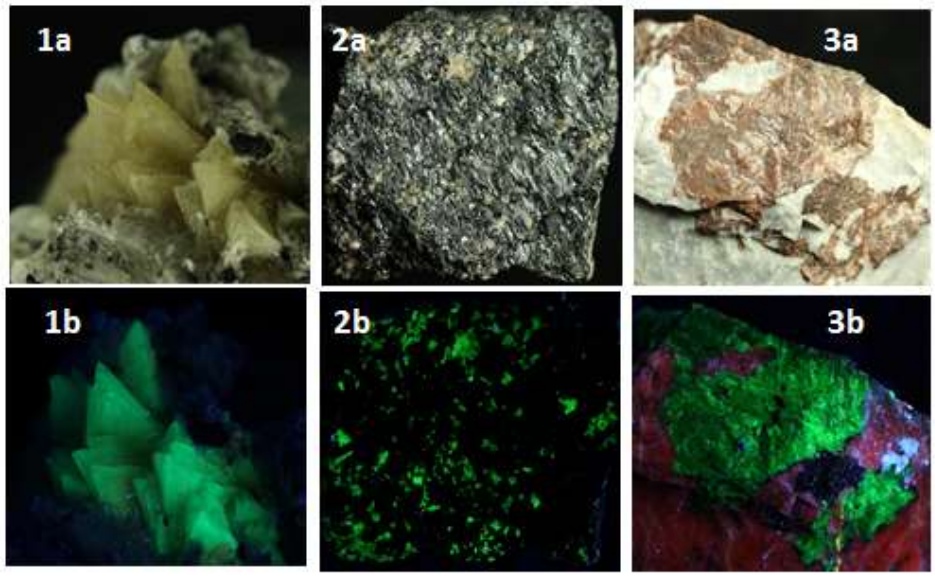

Figure 2. Photos of studied minerals: a—visible light, b—short UV light, 1—genthelvite G1, 2—willemite W2, 3—willemite W1 and calcite.

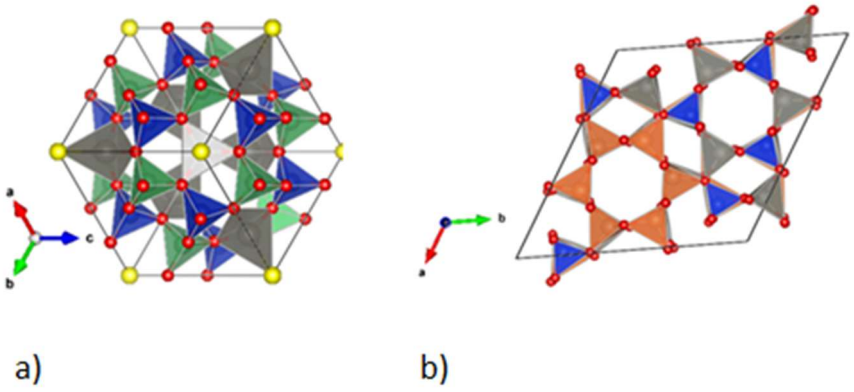

Figure 3. The sketches of the structure of studied minerals using Vesta 3 program and American Mineralogist Crystals Database, (**a**) genthelvite: sulphur—yellow, oxygen—red, ZnO_4—grey, BeO_4—green, SiO_4—blue; (**b**) willemite: Zn_1O_4—orange, Zn_2O_4—grey, SiO_4—blue.

Two willemite Zn_2SiO_4 specimens from the Franklin deposit (Franklin, Sussex County, NJ, USA), were studied here. The first one, named W1, forms a mass of fine grains of a prismatic or lamellar habit and dark red (maroon) color. The second, W2, forms colorless, small—up to 1.5 mm—prismatic crystals (see photos 2a, b). Willemite belongs to orthosilicates, is trigonal, space group $R\bar{3}$, the number of formula unit Z = 18 and lattice parameters refined as the standard [23] are a = 13.948(2) Å, c = 9.315(2) Å, Z = 18. In the references [24,25], the zinc positions are named the opposite of Klaska et al. [23]. The Zn_1 tetrahedrons (orange) are smaller (<Zn_1-O> = 1.9495 Å) than Zn_2 (grey) <Zn_2-O> = 1.9613 Å. Zn_1O_4 tetrahedrons form 6-membered rings with each other and also 4-membered

rings with SiO_4 and Zn_2O_4 tetrahedrons. Zn_2O_4 forms 6-membered rings with SiO_4 and 4-membered rings with SiO_4 and Zn_1O_4 tetrahedrons. The average distances are Zn_1-Zn_1 ~3.14 Å, Zn_1-Zn_2 ~3.50 Å, Zn_2-Zn_2 ~5.25 Å. Each oxygen is bonded to three tetrahedral cations, one silicon (Si^{4+}) and two zinc ($Zn_1{}^{2+}$, $Zn_2{}^{2+}$). All ions occupy an 18*f* position, and the site symmetry of the Zn^{2+} is triclinic C_1. The sketches of the willemite crystal structure are presented in Figure 3b.

The Measurements' Conditions

The preliminary chemical compositions of willemite W1, W2 and genthelvite G1, G2 were examined using a scanning electron microscope Phenom XL equipped with an EDS (energy-dispersive X-ray spectroscopy) detector (Institute of Earth Sciences, Faculty of Natural Sciences, University of Silesia, Sosnowiec, Poland). Quantitative chemical analyses of both minerals were carried out on a CAMECA SX100 electron microprobe (Institute of Geochemistry, Mineralogy, and Petrology, University of Warsaw, Poland) at 15 kV and 10 nA and using the following lines and standards: Si*K*a, Mg*K*a = diopside; Zn*K*a = sphalerite; S*K*a = chalcopyrite; Mn*K*a = rhodonite; Fe*K*a = Fe_2O_3. Beam diameter was 5 μm for willemite and 10 μm for genthelvite.

The powdered sample of genthelvite (G1, G2) and willemite (W1, W2) were examined by X-ray powder diffraction (XRD). A PANalytical PW 3040 diffractometer was used (Bragg-Brentano, theta- theta geometry), using Co Kα1 radiation (filtered by Fe filter placed on the diffracted beam path). The generator settings for the X-ray tube were: tension = 40 kV, current = 40 mA. The measurements conditions were: scan range: 5–110 2θ degree time limit was set to 300 sec, and the scan speed was 0.02 2θ degree. The Rietveld method was applied to refine collected patterns using the HighScore+ software (version 4.9, Malvern Panalytical B.V., Almelo, The Netherlands.

The Raman spectra of genthelvite samples were recorded on a WITec alpha 300R Confocal Raman Microscope equipped with an air-cooled solid laser 532 nm and a CCD (closed-circuit display) camera operating at −61 °C. The laser radiation was coupled to a microscope through a single-mode optical fiber with a diameter of 3.5 μm. An air Zeiss (LD EC Epiplan-Neofluan DIC-100/0.75NA) objective (Carl Zeiss AG, Jena, Germany) was used. Raman scattered light was focused by an effective Pinhole size of about 30 μm and a monochromator with a 600 mm^{-1} grating. Integration times of 5 s with an accumulation of 30 scans and a resolution of 3 cm^{-1} were chosen. The Raman spectra of willemite samples W1 and W2 were recorded on a WITec alpha 300R Confocal Raman Microscope equipped with an air-cooled solid laser 633 nm and a CCD (closed-circuit display) camera operating at −61 °C. The laser radiation was coupled to a microscope through a single-mode optical fibre with a diameter of 50 μm. An air Zeiss (LD EC Epiplan-Neofluan DIC-100/0.75NA) objective) was used. The scattered light was focused on multi-mode fibre (100 μm diameter) and a monochromator with a 600 mm^{-1} grating. Raman spectra were accumulated by 30 scans with an integration time of 20 s and a resolution of 3 cm^{-1}. In both cases, the monochromator was calibrated using the Raman scattering line of a silicon plate (520.7 cm^{-1}).

All Raman spectra processing was performed using the Spectracalc software package GRAMS (Galactic Industries Corporation, Salem, NH, USA), while the baseline correction and cosmic ray removal were conducted using WitecProjectFour software (version Four, WITec Company, Ulm. Germany). The Raman bands were fitted using a Gauss-Lorentz cross-product function with the minimum number of component bands used for the fitting process.

Luminescence spectra were determined at room temperature using a Jobin-Yvon (SPEX) FLUORLOG 3-12 spectrofluorimeter with a 450 W xenon lamp, a double-grating monochromator and a Hamamatsu 928 photomultiplier. Luminescence decay curves were measured utilizing a pulsed excitation delivered by a Continuum Surelite optical parametric oscillator (OPO) pumped with the third harmonic of an Nd:YAG laser. The decays were measured with a Hamamatsu R-955 photomultiplier connected to a Tektronix Model MDO

4054B-3 digital oscilloscope. For low-temperature measurements, samples were placed in a continuous-flow liquid-helium cryostat equipped with a temperature controller.

3. Results and Discussion

3.1. Chemical Analyses

The results of electron microprobe analyses for genthelvite and willemite crystals are presented in Tables 1 and 2, respectively. The obtained results indicate that studied crystals are chemically homogeneous and show extremely little variation in cation content.

Table 1. Chemical composition (wt.%) of genthelvite $Be_3Zn_4(SiO_4)_3S$.

	Sample G1			**Sample G2**		
Constituent	Mean	S.D.	Range	Mean	S.D.	Range
	n = 12			n = 12		
SiO_2	30.74	0.19	30.48–31.11	30.77	0.20	30.44–31.12
BeO	12.70 *			12.70 *		
MnO	1.87	1.54	0.38–5.16	3.36	1.78	1.39–6.77
ZnO	52.22	1.81	49.27–54.71	50.77	1.87	47.56–53.06
S	5.45	0.06	5.32–5.54	5.45	0.01	5.43–5.47
−O = S	−2.72			−2.72		
Total	100.26			100.33		
Calculated on the basis of 13 anions (12O + S)						
Si^{4+}	3.02			3.02		
Be^{2+}	3.00			3.00		
Mn^{2+}	0.16			0.28		
Zn^{2+}	3.79			3.68		
Sum M	3.95			3.96		
S^{2-}	1.00			1.00		

Note: * Calculated on the basis of stoichiometry; S.D. = 1σ = standard deviation; n = number of analyses.

Table 2. Chemical composition (wt.%) of willemite Zn_2SiO_4.

	Sample W1			**Sample W2**		
Constituent	Mean	S.D.	Range	Mean	S.D.	Range
	n = 12			n = 12		
SiO_2	28.37	0.37	27.68–28.85	27.80	0.12	27.53–27.93
FeO	0.29	0.12	0.05–0.50	0.03	0.04	0.00–0.12
MgO	2.38	0.88	0.87–3.30	0.25	0.03	0.20–0.30
MnO	3.40	0.56	2.42–4.25	6.49	0.57	4.91–7.10
ZnO	65.99	1.53	64.10–68.31	65.74	0.77	64.44–67.46
Total	100.43			100.31		
Calculated on the basis of 4 O						
Si^{4+}	1.01			1.01		
Fe^{2+}	0.01			<0.01		
Mg^{2+}	0.13			0.01		
Mn^{2+}	0.10				0.20	
Zn^{2+}	1.74			1.77		
Sum A	1.98			1.98		

Note: S.D. = 1σ = standard deviation; n = number of analyses.

Both studied genthelvite samples are from Mont-Hilaire. The Mn content in these samples is lower than that found by Halenius [22], i.e., 6.27 wt.%, but slightly higher than Hassan and Grundy [21] have shown for crystals from the same locality, i.e., 0.95 wt.%. Moreover, no impurities of other elements such as Fe, Al, Mg, or Ca were found in the tested crystals, as it was demonstrated for different samples, also from other localizations [26,27].

For example, the Mn-content up to 7.66 wt.% and 5.61 wt.% was reported in Fe-poor samples by [28] and [29], respectively. Antao and Hassan [28] found in Mt St. Hilaire genthelvite crystal a two-phase intergrowth with Mn- poor phase, up to 0.14 wt.% and Mn-rich phase contain Mn to 2.45 wt.%.

The Mn-content in crystal G1 is higher than in crystal G2. The empirical formulas of these samples can be written as sample G1: $Be_{3.00}(Zn_{3.68}Mn_{0.28})_{\sum 3.96}Si_{3.02}O_{12}S$, sample G2: $Be_{3.00}(Zn_{3.79}Mn_{0.16})_{\sum 3.95}Si_{3.02}O_{12}S$.

Both studied willemite samples are from Franklin deposit (Franklin, Sussex Cunty NJ, USA). The chemical composition of the W1 sample is more complex than that of sample W2. Whereas the dominant admixture in sample W2, unlike in sample W1, is Mn. The MnO and FeO contents for willemite from Franklin deposit were determined as 0.12–8.96 wt.% and 0.81 wt.%, respectively [29]. For other localities, MnO content was equal to 0.03–1.22 wt.% [27], while FeO up to 0.15 wt.% [30]. The empirical formulas of studied willemite crystals can be written as: sample W1 $(Zn_{1.74}Mg_{0.13}Mn_{0.10}Fe_{0.01})_{\sum 1.98}Si_{1.01}O_4$ and sample W2: $(Zn_{1.77}Mn_{0.20}Mg_{0.01})_{\sum 1.98}Si_{1.01}O_4$.

3.2. XRD Diffraction Patterns

The results of X-ray powder diffraction analyses of studied genthelvite and willemite crystals are presented in Tables 3–5.

The unit parameter a = 8.1090(0) Å of genthelvite was determined by Hassan and Grundy [21] for 0.95 wt.% MnO and a = 8.1493(5) Å for 10.79 wt.% FeO and 1.93 wt.% MnO. For two-phase Mn-poor and Mn-rich intergrowth in genthelvite crystal from the same locality, i.e., Mt. St. Hilaire, the a = 8.119190(7) Å and a = 8.128914(9) Å, respectively [28]. The values of the lattice a parameter measured in the current study correspond to its variability with the content of Mn.

Table 3. Crystal data and data collection information for genthelvite and willemite samples.

Sample	Genthelvite		Willemite	
	G1	G2	W1	W2
Space group (No.)	$P\bar{4}3n$		$R\bar{3}$	
a [Å]	8.12745(3)	8.11944(1)	13.9500(3)	13.9647(2)
b [Å]	8.12745(3)	8.11944(1)	13.9500(3)	13.9647(2)
c [Å]	8.12745(3)	8.11944(1)	9.3254(2)	9.3359(1)
alpha [°]	90	90	90	90
beta [°]	90	90	90	90
gamma [°]	90	90	120	120
V [10^6 pm^3]	536.8626	535.2769	1571.61000	1576.69900
V ESD [10^6 pm^3]	0.002234	0.0008744	0.0474664	0.0290179
R expected	3.420	2.879	7.11093	3.92045
R profile	6.402	6.403	6.63224	5.83627
R weighted profile	9.701	10.074	9.08086	8.53544
GOF	2.837	3.498	1.270	2.177

Klaska et al. [23] measured unit cell parameters for hydrothermal synthesized α-Zn_2SiO_4 to be a = 13.948(2) Å and c = 9.315(2) Å. The unit cell parameters of other synthesized willemite samples are similar: a = 13.9468(3) Å, c = 9.3177(1) Å [25]. For the willemite sample from the Franklin deposit, Simonov et al. [31] have refined its structure and determined a = 13,971(3) Å, c = 9.334(1) Å; however, the content of the impurities was not specified. No other data on the lattice parameters of the willemite mineral have been found in existing literature. For nanocrystalline willemite powder with the highest Mn-content, i.e., $Zn_{1.5}Mn_{0.5}SiO_4$, the following unit cell parameters were measured: a = 13.946(5) Å, c = 9.315(2) Å [32]. Thus, it can only be concluded that the studied samples W1 and W2 satisfy the relation of increasing the values of parameters a and c with an increase of Mn content. It was also checked if Mn uniformly occupy Zn_1 and Zn_2 sites. The EPR data [33] and luminescence results [34] showed a clear preference of the Zn_2 site over

the Zn_1 site in the most common 2:1 ratio. On the other hand, Kim et al. [15] diffraction data showed that for the synthetic Zn_2SiO_4 samples $Zn_{2\_x}Mn_xSiO_4$ ($0.01 \leq x \leq 0.05$), the preference of Zn_2 site over Zn_1 was evaluated to be close to 10, with the best Rietveld refinement and Goodness of Fitting (GOF) parameter equal 2.28.

The samples studied here—willemite W1 and willemite W2—contain much more Mn than was noted in previous publications. The performed calculations for the W1 sample ended with GOF = 1.270 showed that Mn occupies only the Zn_1 site. For the W2 sample, almost equally good fit was obtained for two cases. For the first it was calculated in accordance with Klaska et al. structural model [23], obtained GOF = 2.18 when Mn occupied only Zn_2 site. For the second, with Hang et al. [35] structural data, obtained GOF = 2.17 when 5% Mn and 1% Mg were presented at Zn_1 site, while 95% of Mn occupied Zn_2 site. The calculations put in Tables 4 and 5 show that there is a preference of the lattice sites in both samples and that this preference is different in them.

Table 4. Refined structural parameters for W1 sample $Zn_{1.74}Mg_{0.13}Mn_{0.10}Fe_{0.01})_{\sum 1.98}Si_{1.01}O_4$ obtained from the Rietveld refinement using X-ray powder diffraction data at room temperature.

Atom	Wyck.	s.o.f.	x	y	z	B × 10^4 (pm^2)
Zn1	18f	0.76(5)	0.017430	0.209100	0.084650	0.511026
Zn2	18f	1.000000	0.023060	0.215030	0.418600	0.518746
Si	18f	1.000000	0.211640	0.195570	0.249400	0.218623
O1	18f	1.000000	0.106000	0.216400	0.250500	0.513483
O2	18f	1.000000	0.344670	0.015530	0.084330	0.689644
O3	18f	1.000000	0.209200	0.125600	0.392600	0.496288
O4	18f	1.000000	0.205600	0.128300	0.103600	0.657360
Mn1	18f	0.10(2)	0.017430	0.209100	0.084650	0.511026
Mg1	18f	0.14(5)	0.017430	0.209100	0.084650	0.511026
Fe1	18f	0.02(1)	0.017430	0.209100	0.084650	0.511026

W.P.—Wyckoff position; s.o.f.—site occupation factor; B—isotropic atomic displacement.

Table 5. Refined structural parameters for W2 sample $Zn_{1.77}Mn_{0.20}Mg_{0.01})_{\sum 1.98}Si_{1.01}O_4$ obtained from the Rietveld refinement using X-ray powder diffraction data at room temperature.

Atom	W.P.	s.o.f.	x	y	z	B × 10^4 (pm^2)
Zn1	18f	0.96(9)	0.017100	0.208700	0.084400	0.000000
Zn2	18f	0.91(9)	0.023400	0.215500	0.418500	0.000000
Si	18f	1.000000	0.211800	0.196300	0.249000	0.709822
O1	18f	1.000000	0.208500	0.126700	0.391800	0.850365
O2	18f	1.000000	0.205900	0.129500	0.104500	0.769829
O3	18f	1.000000	0.107500	0.217500	0.249600	0.799833
O4	18f	1.000000	0.345170	0.016830	0.082630	0.990119
Mg1	18f	0.004(2)	0.017100	0.208700	0.084400	0.000000
Mn2	18f	0.17(1)	0.023400	0.215500	0.418500	0.000000
Mn1	18f	0.06(3)	0.017100	0.208700	0.084400	0.000000

W.P.—Wyckoff position; s.o.f.—site occupation factor; B—isotropic atomic displacement.

3.3. Raman Spectra

Until now, the Raman spectra of genthelvite have been cited on the rruff.info website (https://rruff.info/genthelvite/display=default/ on 15 September 2021) and this is the only source material. In literature, there is no description or even qualitative characteristics of the spectrum of this mineral. In genthelvite lattice, three types of tetrahedron BeO_4, ZnO_4, and SiO_4 form a skeleton connecting by oxygen corners. Genthelvite $Be_3Zn_4(SiO_4)_3S$ belongs to tectosilicate, and it is a member of helvine group $Be_3M_4(SiO_4)_3S$ (M = Fe^{2+}, Mn^{2+} and Zn^{2+}) together with danalite ($Be_3Fe^{2+}{}_4(SiO_4)_3S$) and tugtupite ($Na_4BeAlSi_4O_{12}Cl$). Genthelvite can be considered as a member of the sodalite subgroup where Be is playing the role of Al in sodalite $Na_4(Si_3Al_3)O_{12}Cl$ lattice. In genthelvite structure, the number of formula units per unit cell Z = 2, so then 138 normal modes are predicted to $P\bar{4}3n$ space

group. Nevertheless, carrying out the vibration analysis group factor is not the purpose of this work. For this reason, a simplification was adopted to separate the vibrational bands into those originating from the isolated SiO_4^{4-} and (Zn, Mn)O_4^{6-} and BeO_4^{6-} tetrahedrons with T_d point symmetry and into lattice vibrations. For the interpretation of the genthelvite spectra, comparisons with the spectra of sodalite [36] and minerals containing the BeO_4^{6-} anion [37,38] were used. A similar situation occurs in the case of the mineral willemite Zn_2SiO_4 and the availability of spectroscopic data in the literature. Generally, the Raman data for synthetic Zn_2SiO_4 ceramic powders or nanocomposites doped with ions such as Mn^{2+}, Ni^{2+} or Cr^{3+}, Eu^{3+} Er^{3+} and obtained by a sol-gel method are noted [39–45]. Willemite is an orthosilicate mineral, whose crystal structure is composed of SiO_4 tetrahedra and Zn-cations also in tetrahedral coordination. Factor group analysis of willemite structure with the space group $R\bar{3}$ suggests that there are 378 normal modes. As was the case above, the interpretation of the willemite Raman spectrum focuses on vibrational bands from the isolated SiO_4^{4-} and (Zn, Mn)O_4^{6-} tetrahedrons with T_d point symmetry and on lattice vibrations.

The most intense bands in Raman spectra of genthelvite and willemite come from SiO_4 tetrahedra because the Si-O bond is the most covalent one. Both studied minerals have SiO_4 and ZnO_4 tetrahedrons, in genthelvite also BeO_4 tetrahedrons, thus, the Raman spectra may show some similarities as well as differences. Therefore, the following qualitative description of Raman spectra of the studied minerals is proposed. The two genthelvite samples G1 and G2 are from the same locality (Mont Saint-Hilaire in Quebec, QC, Canada) and differ in Mn content (Table 1). The Raman spectra of the studied genthelvite are showed in Figure 4. The differences in the number, frequency, and intensity of the bands in both spectra are infinitesimally small, practically negligible. The most intense band at 887 cm^{-1} is assigned to Si-O stretching υ_1(A) vibration. The four bands on the higher frequency side (911–1031 cm^{-1}) can be identified as asymmetric stretching Si-O band $\upsilon_3(F_2)$. The bands at 609–635 cm^{-1} and 418–445 cm^{-1} could be assigned as Si-O bending υ_4 and υ_2 vibrations, respectively. In turn, the ZnO_4 tetrahedron υ_3, and υ_1 vibration could be recognized at 609–635 cm^{-1} and 539 cm^{-1}, respectively. The bands at 575 cm^{-1} and 773 cm^{-1}, which are not present in willemite spectra (Figure 5), could be recognized as symmetric υ_1 and asymmetric υ_3 stretching vibrations related to the BeO_4 tetrahedrons [37,40,46,47]. A very intensive band is visible at 170 cm^{-1}, the lack of which in the willemite spectra and measured for helvine (https://rruff.info/helvine/display=default/ on 15 September 2021) and danalite (https://rruff.info/danalite/display=default/ on 15 September 2021) should be attributed to the Be-O vibrations.

The Raman spectroscopic analyses for two willemite samples (sample W1 and W2) from Franklin Mining District, Sussex County, NJ, USA, were performed, and the spectra are showed in Figure 5. Chemically, the samples differentiate in Mn, Mg, and Fe contents (Table 2). The most intense band noted in the spectra and centred at 874 cm^{-1} is assigned to the symmetric Si-O stretching υ_1(A) vibration. Three bands in the range 900–950 cm^{-1}, respectively at 903, 911, 951 cm^{-1} for sample W1 and 904, 910, 949 cm^{-1} for sample W2, are ascribed to the υ_3 (F_2) triply degenerate asymmetric stretching vibrations. The symmetric υ_2 (E) and asymmetric υ_4 (F_2) bending O-Si-O vibrations are observed in ranges 380–400 cm^{-1} and 470–510 cm^{-1}, respectively. The assignation of the vibrations of $(SiO_4)^{4-}$ groups in willemite samples from Franklin are in good agreement with Handke and Urban [48] for other orthosilicates [49–51]. The presence of a single band at 552 cm^{-1} (sample W1) and 548 cm^{-1} (sample W2), as well as bands in the range 600–625 cm^{-1}, is disputable and not completely defined. Based on willemite IR spectroscopy results, we can assume that these bands could be assigned to symmetric stretching υ_1 (~550 cm^{-1}) and asymmetric stretching υ_3 vibrations of ZnO_4 [43,45,52]. According to Griffith's work [53], band ~550 cm^{-1} can also be related to asymmetric bending vibrations, where υ_4 was at 542 cm^{-1} [53], but in present work, this band is shifted to the higher wavenumbers. In both samples, Zn is replaced by atoms of lower mass with a similar total amount. However, there is more Mg than Mn in sample W1, hence the frequency of υ_1 ZnO_4 is higher (552 cm^{-1}) than for

sample W2. The W1 sample has more atoms which are lighter than Zn, and shorter Zn-O bond lengths, than sample W2, which resulted in a higher frequency of the υ_1 band than for sample W2, i.e., 552 cm^{-1} and 548 cm^{-1}, respectively. The deconvolution of the υ_3 band into its components looks different for the two samples. There are bands at 597 and 623 cm^{-1} for W1 and 602 and 626 cm^{-1} for the W2 sample, which is undoubtedly related to the different lattice sites occupation by Mn in these samples. In the lattice vibrations range, a slight distinction in the number or intensity of the bands can be noticed, which may be related to the differences in the content of impurity elements. The spectrum of willemite W2 in the range of lattice vibrations shows bands with frequencies 217 and 237 cm^{-1}, not measured for sample W1. They probably come from $Mn(Zn_2)$-O vibrations.

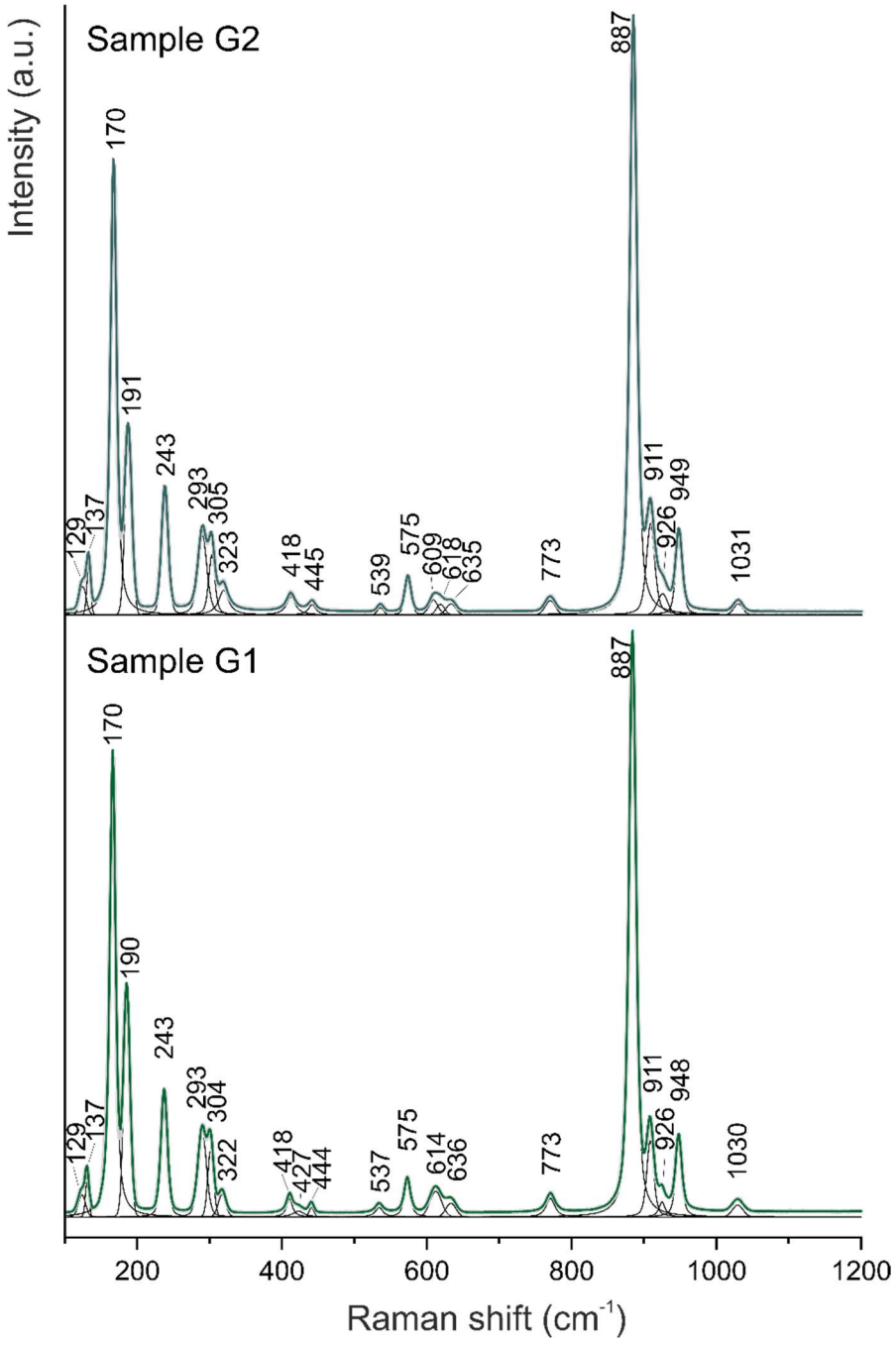

Figure 4. Raman spectra of genthelvite samples.

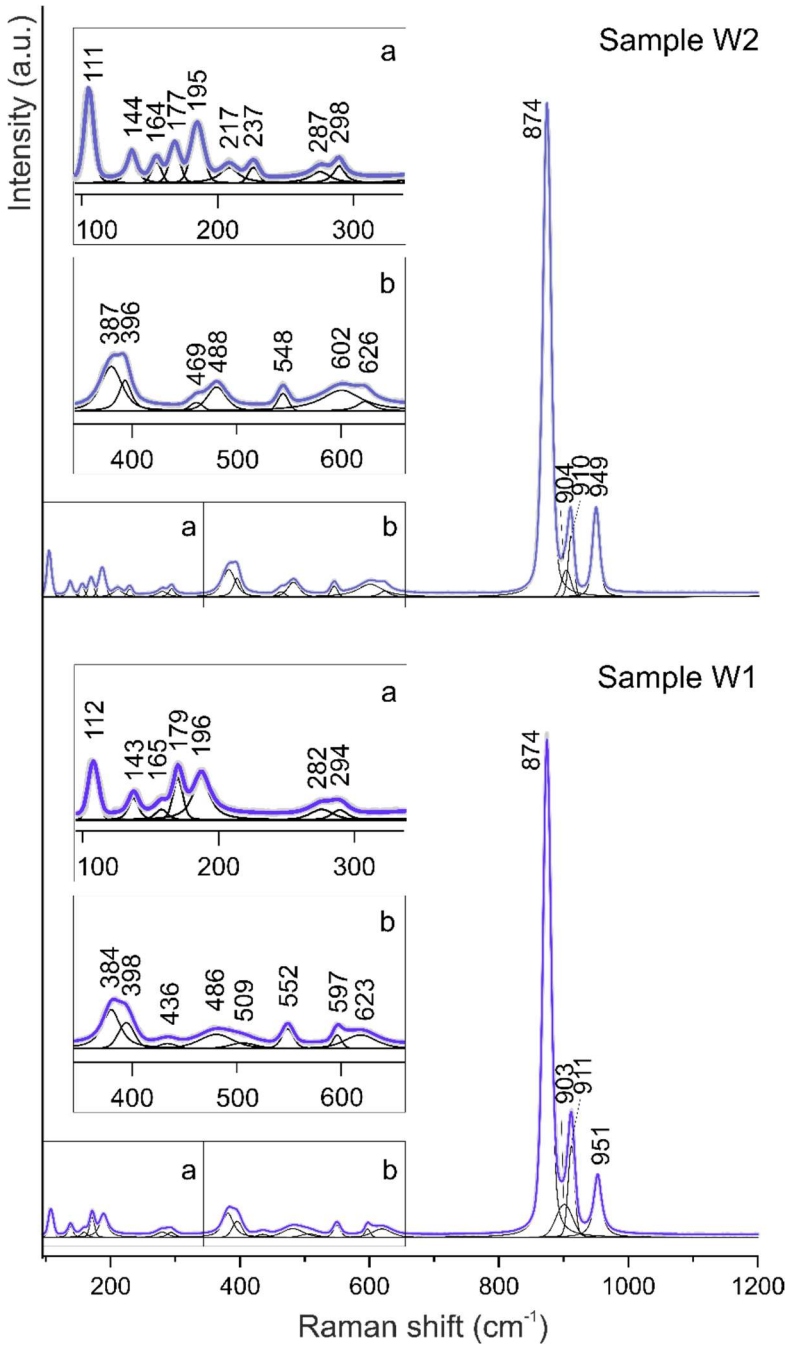

Figure 5. Raman spectra of willemite samples.

The Raman bands position and their assignment for genthelvite and willemite samples are indicated in Table 6.

The difference in the masses of atoms of the tetrahedrons adjacent to SiO_4 may influence the value of the frequency of Si-O vibrations. In genthelvite, for the SiO_4 tetrahedron, each apex oxygen is also common to the two BeO_4 and ZnO_4 tetrahedrons. While the former neighborhood may cause an increase in the frequency, the latter one decreases it. The reduced masses for the Si-Be, Si-Zn and Si-Si pair are 0.1465 and 0.0509 and 0.0712, respectively. It means that the neighborhood of Be, which increases the frequency, has greater influence. Indeed, vibrations of SiO_4 tetrahedron have higher frequencies for genthelvite (887 cm^{-1}, 418–445 cm^{-1}) than for willemite (874 cm^{-1}, 387–448 cm^{-1}). In addition, in the range below 300 cm^{-1}, a greater number of bands were measured for the willemite, usually with a lower relative intensity than for the genthelvite.

Table 6. Raman bands (position and assignment) of studied genthelvite and willemite samples.

Bands Position (cm^{-1})		Assignation	Bands Position (cm^{-1})		Assignation
Sample G1	**Sample G2**		**Sample W1**	**Sample W2**	
1030 948 926 911	1031 949 926 911	υ_3 (F_3) Si-O stretching	951 911 903	949 910 904	υ_3 (F_3) Si-O stretching
887	887	υ_1 (A) Si-O stretching	874	874	υ_1 (A) Si-O stretching
773	773	υ_3 (F_3) Be-O stretching	-	-	
636 614	635 618 609	υ_4 (F_3) O-Si-O bending	623 597	626 602	υ_3 (F_3) Zn-O stretching
575	575	υ_1 (A) Be-O stretching	-	-	
537	539	υ_1 (A) Zn-O stretching	552	548	υ_1 (A) Zn-O stretching
444 427 418	445 418	υ_2 (*E*) O-Si-O bending	509 486	488 469	υ_4 (F_3) O-Si-O bending
			436	-	unknown
			398 384	396 387	υ_2 (*E*) O-Si-O bending
322 304 293 243 190 137 129	323 305 293 243 191 137 129	Lattice vibrations	294 282 196 179 165 143 112	298 287 237 217 195 177 164 144 111	Lattice vibrations
170	170	Be-O			

3.4. Luminescence Spectra

3.4.1. Genthelvite

The emission and excitation spectra of the genthelvite G1 sample have been presented in Figure 6. At room temperature, the emission band was measured at λ = 508 nm, the full width at half maximum (FWHM) was 844 cm^{-1}. At low temperature (T = 77 K), the emission band became narrower, FHHM = 655 cm^{-1} and asymmetrical from a longer wavelength. It could be related to lattice vibration; however, its maximum was measured at the same position, i.e., λ = 509 nm. At the same time, no significant shift of the excitation bands was found. The υ_3 band is single also at low temperature (see inset in Figure 6a). It is worth noting that the υ_2 band is wider than the υ_3 band; full width at half maximum (FWHM) is equal to 460 cm^{-1} and 140 cm^{-1}, respectively. Due to the interactions with phonons, the υ_5, υ_4, and υ_2 bands at T = 77 K have a complex shape with a shoulder as a result of coupling with the intense lattice vibrations at 170 cm^{-1} (Figure 4). The position of the υ_1 band is not precisely measured due to its proximity to the emission band. The

emission and excitation spectra for the genthelvite G2 sample were the same as for the G1 sample. Gorobets and Rogojine [54] measured the Mn^{2+} emission band for genthelvite at 510 nm. The measured lifetimes of luminescence have values expected for spin-forbidden transition $^4T_1(^4G) \rightarrow {}^6A_1(^6S)$. Their values equal 2.20 ms and 3.4 ms for samples G1 and G2 increased to 2.63 ms and 4.51 ms as the temperature was decreased (Figure 7). It means that that thermal quenching of the decay time takes place. A brief discussion of the luminescence decay times is included in Section 4.

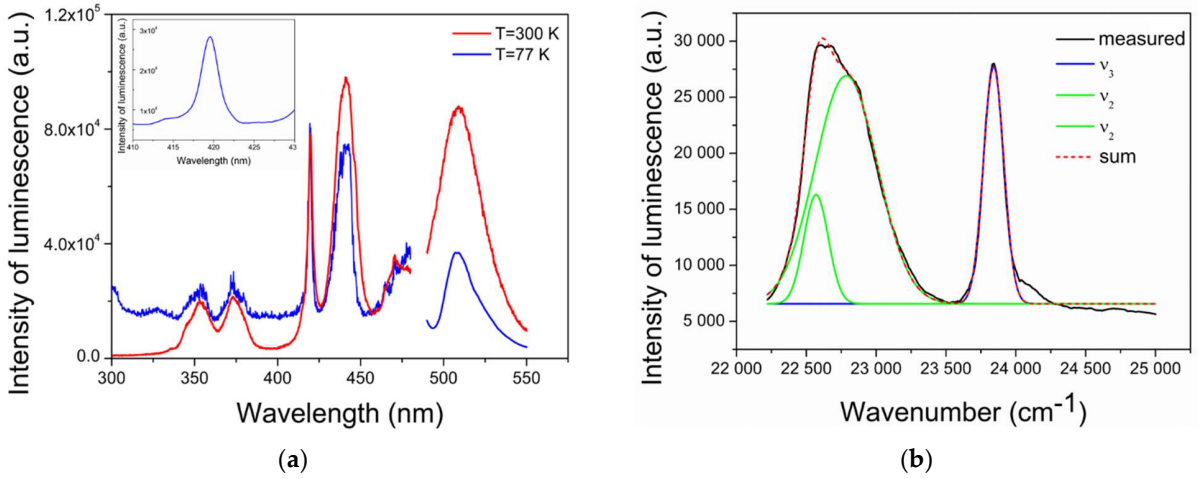

(**a**) (**b**)

Figure 6. Luminescence spectra of Mn^{2+} in genthelvite, (**a**) left—excitation spectrum, right—emission spectrum. Inset: the υ_3 excitation band measured at T = 77 K; (**b**) deconvolution of the υ_3 and υ_2 excitation bands measured at T = 77 K.

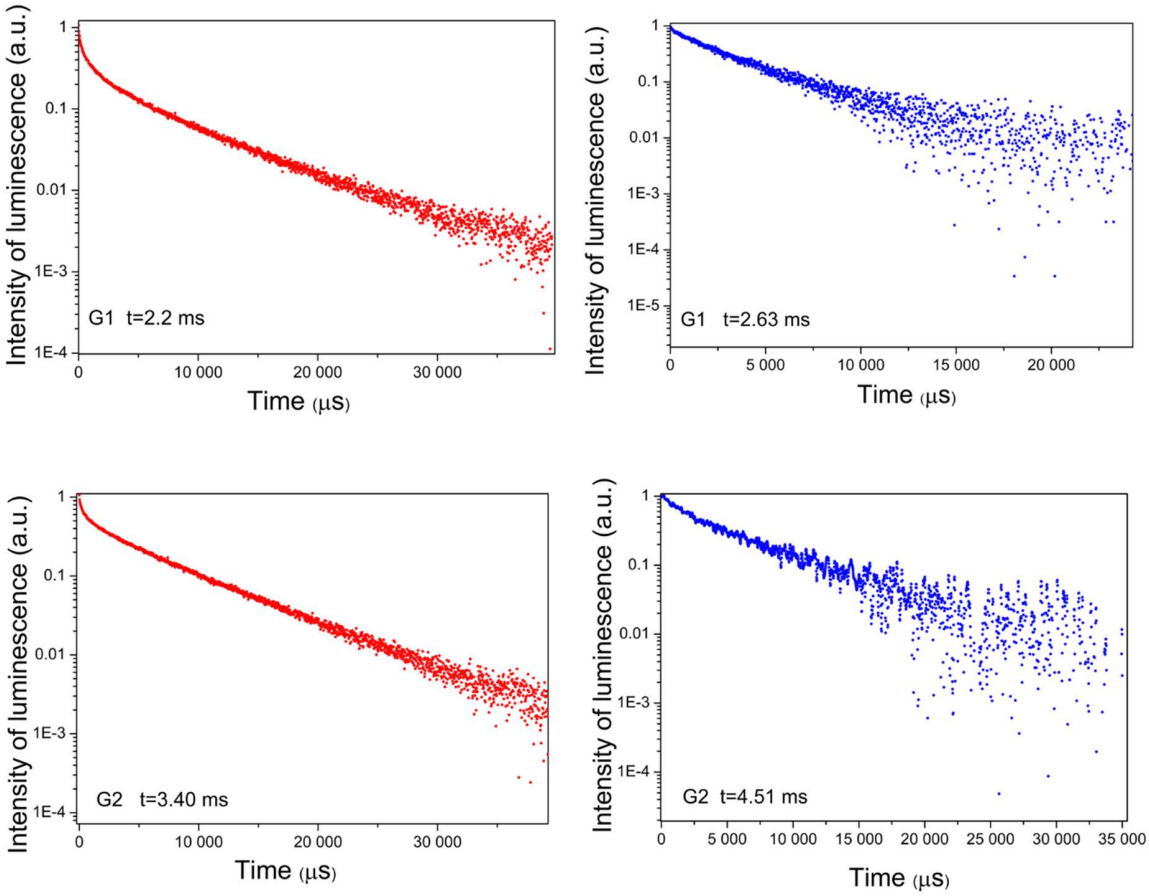

Figure 7. Luminescence decay curves for genthelvite samples G1 and G2 measured at T = 300 K and T = 77 K (red and blue line, respectively).

3.4.2. Willemite

Mn-doped Zn_2SiO_4 green phosphor is of particular interest because of its high luminescence efficiency, high photo-stability (especially under UV excitation), and stability to moisture. The alpha (rhombohedral) and beta (orthorhombic) Zn_2SiO_4 phases were synthesized by various methods, which often produce nanoparticles or thin films. For example, Bertail et al. [55] showed the maximum of luminescence efficiency and the longest luminescence lifetime 35 ms for the $Zn_{1.6}Mn_{0.4}SiO_4$ sample. Rivera-Enríquez et al. [56] found that the optimal Mn dopant concentration for the α-Zn_2SiO_4 samples is approximately 3 mol%, and the decay time was determined to be 10.93 ms. The luminescence decay curves have been fitted to the double-exponential decay function. Kretov et al. [57] estimated luminescence lifetime for α-willemite with 0.7 Mn mol% to be 22 ms. The emission measurement conducted at T = 4 K [34] showed two Zero-Phonon lines (ZPL) of Mn^{2+} emission at 18,673 cm^{-1} (535 nm; 2.32 eV) and 19,675 cm^{-1} (508 nm; 2.44 eV) from Zn_2 and Zn_1 site. The ratio of the intensity of this second line to the intensity of the higher energy line was 1: 2–2.5 and did not change after heat treatment of the sample. They believed [57] that the emission band measured for T = 300 K and T = 77 K at 525 nm (19,047 cm^{-1}) is the sum of these two components. Since the higher emission energy of Mn^{2+} corresponds to the lower value of *Dq*, i.e., the greater length of the Mn-O bond, i.e., corresponds to the Zn_2 site. Moreover, their measurements and calculations have shown that up to 0.7 wt.% of Mn, the occupancy ratio Zn_2:Zn_1~2 as was earlier demonstrated by EPR measurement [33].

Mineral willemite fluoresces brilliant, intense green, sometimes yellow-green. On several websites, some photos and data could be seen on, for example: http://www.fluomin.org/uk/fiche.php?id=199 (on 10 September 2021). A single and intense emission band at 525 nm was measured as $^4T_1(^4G) \rightarrow {}^6A_1(^6S)$ transition. The intensity of this emission is slightly higher for the sample containing more Mn, i.e., for the W2 sample. The emission bands are a bit asymmetric (Figure 8). The distribution of these bands into its components is as follows: for sample W1, first maximum at 528 nm (18,927 cm^{-1}) and FWHM = 1166 cm^{-1} and the second at 523 nm (19,120 cm^{-1}) and FWHM = 397 cm^{-1}. The second band can be recognized as the sum of the electronic transition, i.e., 18.927 cm^{-1} and lattice vibrations at 196 cm^{-1} (see Figure 5). The emission band of sample W2 is more symmetrical. The decomposition of the W2 emission band is as follows: the first component at 523 nm (19,133 cm^{-1}) and FWHM = 603 cm^{-1} and the second at 535 nm (18,663 cm^{-1}) and FWHM = 1365 cm^{-1}. Due to the nature of the fitting of this band, the component lines can be regarded as the sum (18,663 cm^{-1} + 237cm^{-1} = 18,900 cm^{-1} and the difference (19,133 cm^{-1} − 217cm^{-1} = 18,916 cm^{-1}) the emission band at about 18,900 cm^{-1} (529 nm) with lattice Mn-O vibrations at 217 cm^{-1} and 237 cm^{-1}. There is a visible difference in the coupling of the electronic transition with vibrations for both subjects. At the present stage of research, the reasons for this cannot be established. The W1 and W2 samples differ in the amount of Mn and its different incorporations into the willemite structure. However, it is not known whether and how these factors caused the observed differences.

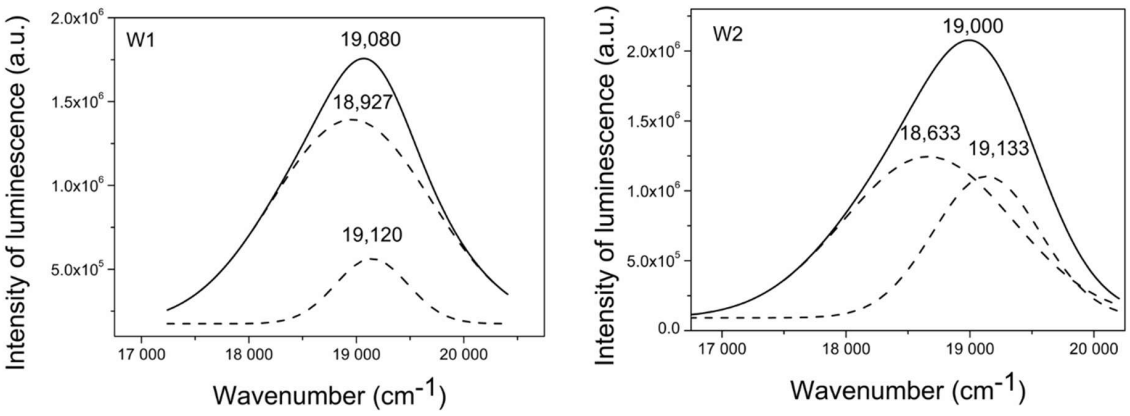

Figure 8. Deconvolution of the Mn^{2+} emission band for W1 and W2 samples.

The energy of Mn^{2+} transitions measured for natural and synthetic $ZnSiO_4$ and calculated in the earlier studied was put in Table 7. The excitation spectra of samples W1 and W2, although similar, are not identical. For current researches, the emission and excitation spectra of willemite measured at room and liquid nitrogen temperatures have been presented in Figures 9–12. The υ_3, υ_4, and υ_4 and υ_1 band are not identical, as is clearly visible on the excitation spectrum measured at T = 77 K (Figures 9d and 11a). Splitting of some absorption bands on the absorption spectrum of Mn^{2+}-bearing willemite has been measured by Halenius [9], as well as on the excitation spectrum of synthetic Zn_2SiO_4: Mn by Palumbo and Brown [14]. However, the authors give different reasons for this splitting. Palumbo and Brown [14] noticed the splitting not only of υ_1, υ_2, and υ_4 but also of υ_3 and υ_5 bands, which correspond to transitions independent of *Dq*. They considered the low site symmetry of the Mn^{2+} in the willemite structure as the reason for this effect. The willemite W2 and W1 samples are a case of evident splitting the $^4E^4A_1(^4G)$ level and with a very high value ΔE = 577 cm^{-1} and 598 cm^{-1}, respectively. At T = 300 K, the level $^4E^4A(^4G)$ splits into two components, while at T = 77 K it splits into three.

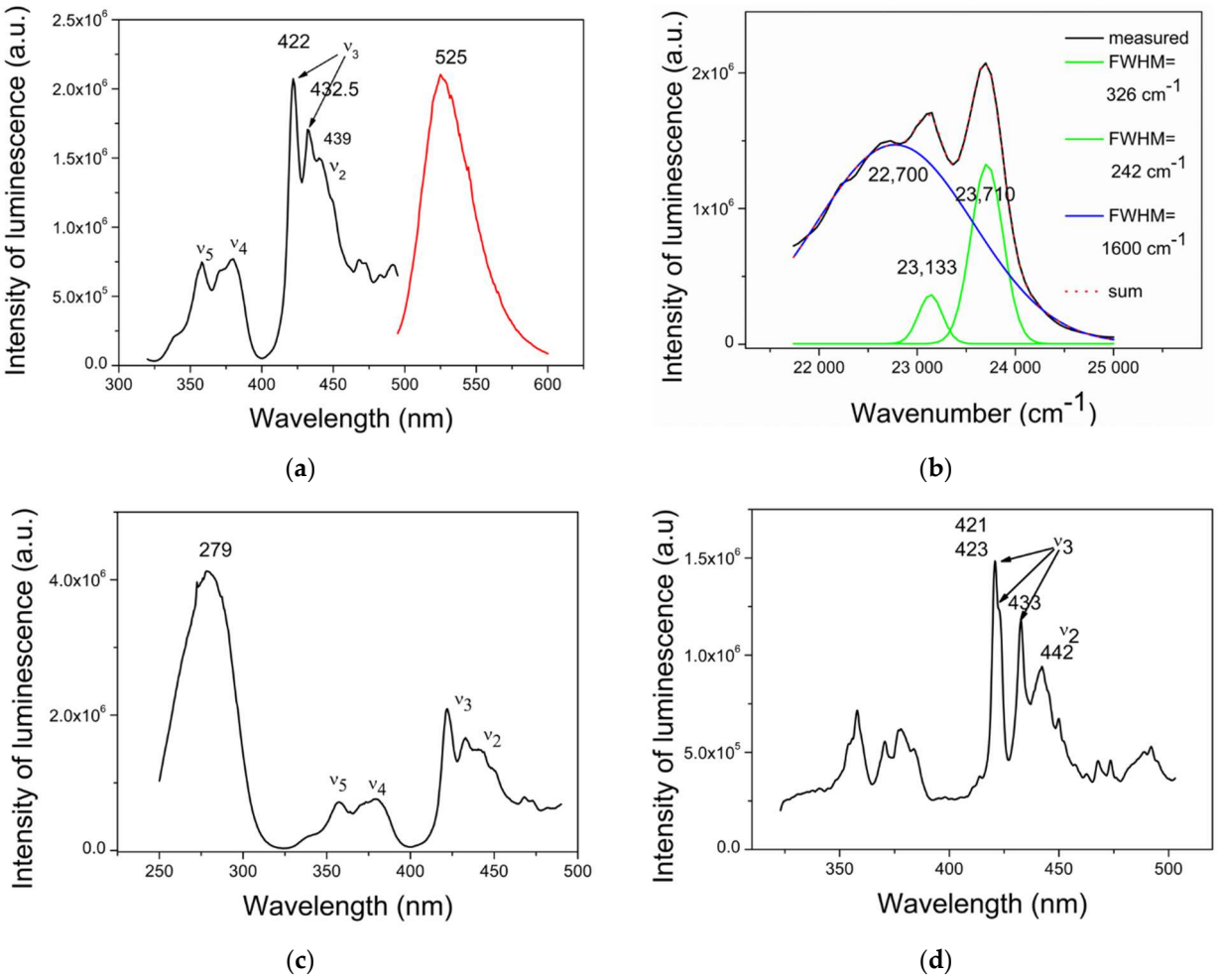

Figure 9. Luminescence spectra of willemite W2 sample: (**a**) emission (right) and excitation (left) of Mn^{2+} measured at T = 300 K; (**b**) deconvolution of υ_2 and υ_3 bands; (**c**) excitation spectrum for λ = 525 nm—point defect to Mn^{2+} energy transfer; (**d**) luminescence excitation spectrum measured at T = 77 K.

The intense band measured on the excitation spectrum at 279 nm (Figure 9c) is the charge transfer (CT) transition from the ground state $^6A_1(^6S)$ of Mn^{2+} to the conduction band of Zn_2SiO_4. It is a smaller energy gap value than the theoretically calculated or determined from the absorption edge. Probably in natural crystals, there are levels below

the Fermi surface and associated with point defects, hence the lower value than 260 nm, i.e., 4.76 eV [58].

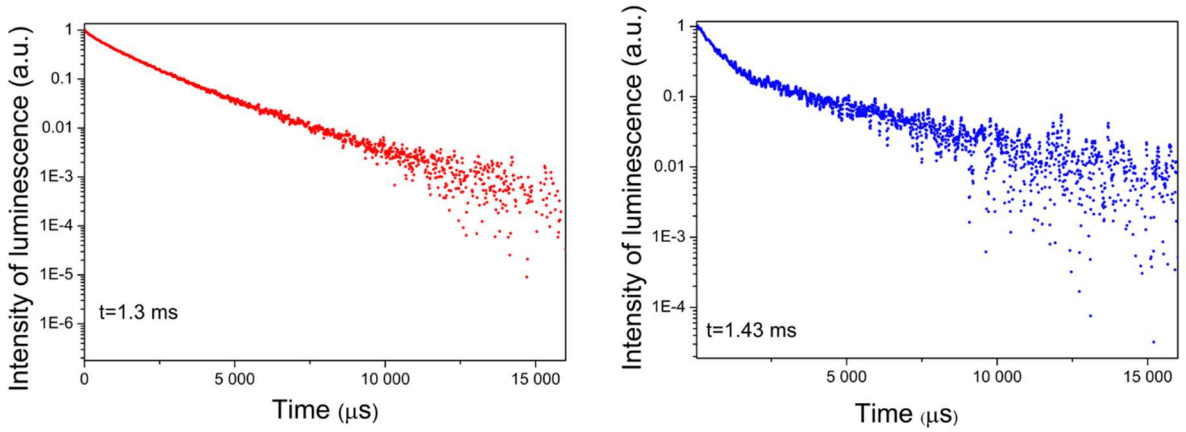

Figure 10. Luminescence decay curves for willemite sample W2 measured at T = 300 K and T = 77 K (red and blue line, respectively).

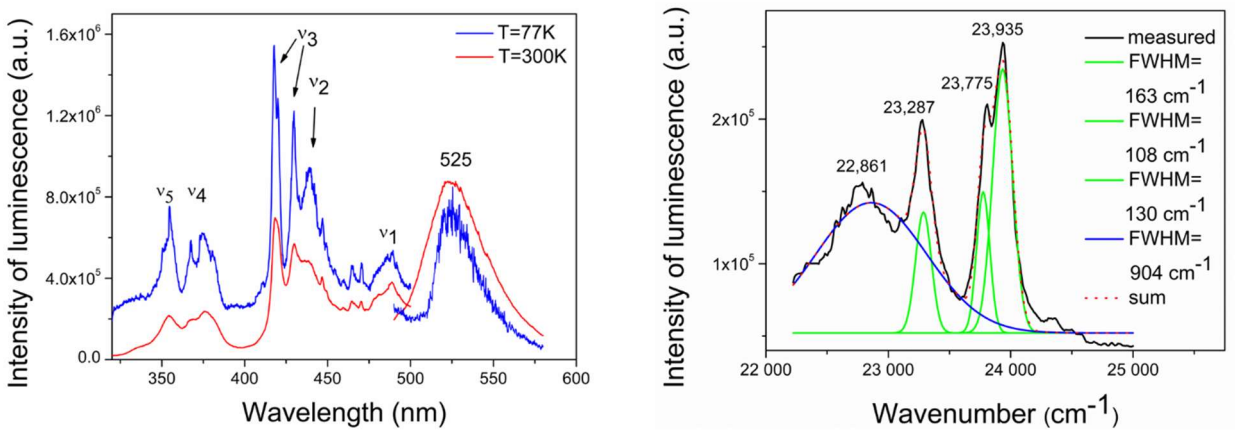

Figure 11. Luminescence spectra of willemite W1 sample: (**a**) emission and excitation of Mn^{2+} measured at T = 300 K and T = 77 K; (**b**) deconvolution of υ_2 and υ_3 bands.

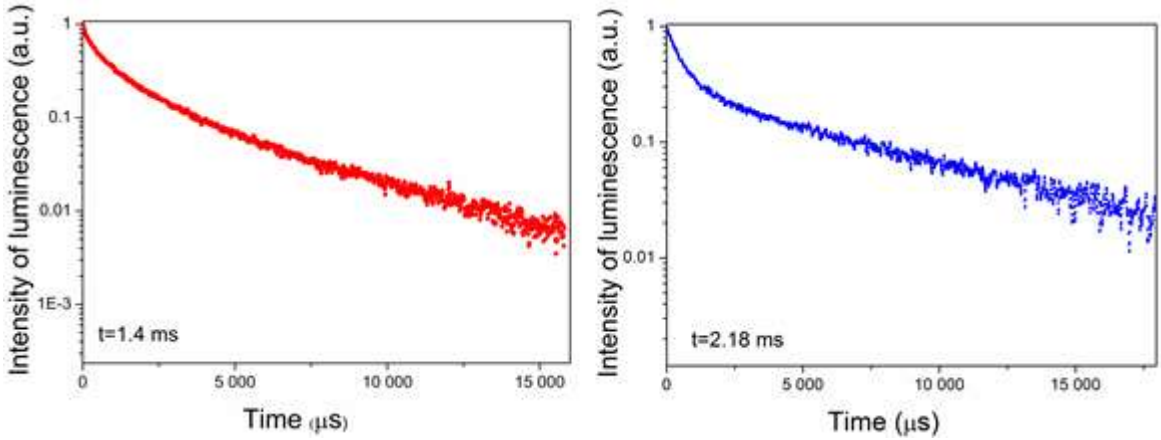

Figure 12. Luminescence decay curves for willemite sample W1 measured at T = 300 K and T = 77 K (red and blue line, respectively).

The measured luminescence lifetimes of both W2 and W1 samples are typical for Mn^{2+} emission (Figures 10 and 12). The lifetimes of sample W2 are shorter than those of sample W1. A proposal to explain the differences in the measured luminescence decay times is provided in Section 4.

Table 7. The measured and calculated Mn^{2+}-bands for natural and synthetic willemite.

Transitions (cm^{-1})	Zn_2SiO_4-Willemite Mineral				Synthetic Zn_2SiO_4						
	Halenius et al. [7]	Current Study W1 Sample Excitation		Palumbo and Brown [14]	Vaida [18]		Curie et al. [12]			Su et al. [20]	
					Measured	Calculated	Measured	Calculated = 65 cm^{-1}		Measured	Calculated
	T = 300 K	T = 300K	T = 77 K		T = 300 K			ε = 0.0	ε = 0.113	T 300 K Equation (1)	
$^6A_1(^6S) \rightarrow {}^4T_1(^4G)$	20,370 21,230	20,462 20,811	20,462 20,794	20,109 20,475 21,035	20,911	20,017 20,461 20,649	20,540	20,449	20,563	20,367	20,465 ± 500
$^6A_1(^6S) \rightarrow {}^4T_2(^4G)$	22,700 23,120	22,820	22,771	22,573 23,095	22,974	21,531 22,411	22,834	22,981	22,420	23,095	22,648 ± 600
$^6A_1(^6S) \rightarrow {}^4E,{}^4A_1(^4G)$	23,700	23,279 23,877	23,287 23,775 23,935	23,640 23,764 23,787	23,704	23,332 24,705 24,750	23,730	23,754 23,754	23,969 23,186	23,736	23,740 ± 450
ΔE	Not observed	598	663	147	Not observed	1418	Not observed	0	783	Not observed	Not calculated
$^6A_1(^6S) \rightarrow {}^4T_1(^4D)$	26,320 27,070	26,550 27,211	26,212 26,671 27,225	25,967 26,932	26,539	26,164 27,794 27,853	26,423	27,405	26,578	26,316	-
$^6A_1(^6S) \rightarrow {}^4E(^4D)$	28,010	28,221	28,136 28,288	27,949 28,985	27,893	29,373 29,900	28,467	28,492	29,302	28,050	28,090 ± 590

3.4.3. Is the υ_2 Band Double?

The luminescence spectra of the willemite W2 sample, measured at T = 300 K and 77 K, were presented in Figure 9, and the positions of its bands are indicated in Table 9. Due to the existence of two non-equivalent lattice sites in the willemite structure, it should be verified whether the measured excitation spectra confirm the Halenius thesis [9], mentioned in Section 1. The excitation spectrum of sample W2 was chosen the first for this discussion as its MnO content is almost the same as for the willemite sample studied by Halenius [9]. The values of the Mn^{2+} absorption bands measured by him are presented in Tables 7 and 10. It has been shown [9] that the bands from υ_1, υ_2, and υ_4 transitions depending on the strength of the crystal field are not single but double. In particular, two υ_2 bands, at 22,700 cm^{-1} and 23,120 $cm^{-1,}$ have been distinguished as corresponding to the different crystal sites with Dq = 551 cm^{-1} and 586 cm^{-1}, respectively. For this reason, for the W2 willemite sample, it is necessary to decide whether or not the band at 22,770 cm^{-1} is the sole υ_2 band or one of the two, the other possible band being the one at 23,133 cm^{-1}.

This assumption was found to be incorrect. The following data support this conclusion: (a) firstly, FWHM of bands at 422 nm (23,710 cm^{-1}) and 432.5 nm (23,133) are similar (326 cm^{-1} and 242 cm^{-1}) but quite different than that band at 439 nm (22,770 cm^{-1}), i.e., (1600 cm^{-1}) (see Figure 9b); (b) secondly, when the 23,133 cm^{-1} band was assumed to be the υ_2 band from the other crystal site, the calculated Dq_2 value was equal 417 cm^{-1} (Table 9). Consequently, Dq_2/B = 0.68, so the predicted emission band should have much higher energy and fall on about 472 nm. No emission band for such a short wavelength has been measured for willemite (dashed green line in Figure 13). For the sample W1 the υ_2 band is not double either. In particular, the additional υ_2 band for this sample is not the band at 429 nm (23,287 cm^{-1}). The justification for this is similar to those for sample W2. One only needs to compare the FWHM of the band's component (Figure 11b) and the estimated value of the emission band from this hypothetical second lattice position. If we assume the 23,287 cm^{-1} as the υ_2 band of hypothetical T2 MnO_4 tetrahedron, then Dq = 425.6 cm^{-1} and Dq/B = 0.68, then the expected emission band should fall on about 474 nm (Table 10). No emission band for such a short wavelength has been measured for this sample. These incorrect emission bands for W2 and W1 samples were marked in Figure 13 as dashed maroon and green lines, respectively. A discussion on the determined Dq and B parameters is developed in Section 3.5.2.

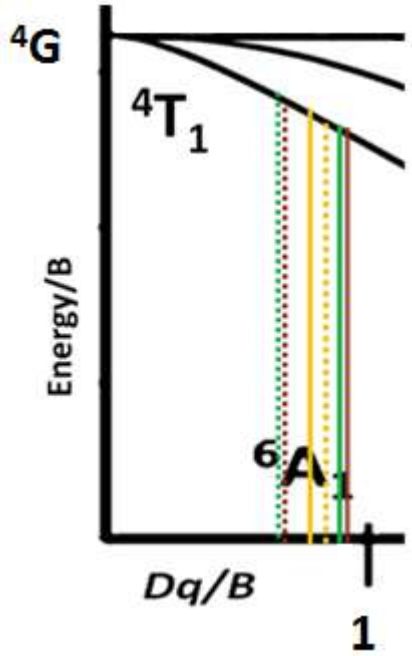

Figure 13. Part of the Tanabe–Sugano diagram; genthelvite G1—yellow lines, willemite W1—maroon line, willemite W2—green lines; solid lines continuous lines for Dq/B cases calculated from Formula (1), dashed line according to the text: yellow line for covalent bond participation, Formulas (4) and (5) from Table 8, green line—for Dq_2 in Table 9, wine line—for Dq_2 in Table 10.

3.5. Calculations of Dq, Racah B and C Parameters, the Energy of Excited Levels, and Split the $^4E^4A_1(^4G)$ Level

The value of the Dq parameter calculated from the position of band υ_1 is burdened with a more significant error than those determined from the position of band υ_2. It should be mentioned that the $^6A_1$–$^4T_1$ transition is forbidden by the group selection rules, whereas the $^6A_1$–$^4T_2$ is allowed. Due to this circumstance, the precise experimental determination of the $^4T_1$ level position from the excitation spectrum is rather ambiguous. Moreover, the υ_1 band is often less visible because it is strongly coupled with lattice vibration; it is very close to Stokes shift associated with the strongest lattice vibration 900 cm^{-1} for genthelvite, 870 cm^{-1}, and 850 cm^{-1} for willemite W1 and W2 samples, respectively. For this reason, in present research, the Dq values were determined from the υ_2 band. A more appropriate Equation (2) was used.

In Figure 13, the Dq/B and $^4T_{1g}(^4G) \rightarrow {}^6A_1(S)$ transitions for genthelvite and two willemite samples are shown schematically.

3.5.1. Genthelvite

Using Tanabe–Sugano Formula (1) for data at T = 300 K it was calculated that B = 633 cm^{-1}, C = 3497 cm^{-1} and $10Dq$ = 5305 cm^{-1} (Table 8). Then nephelauxetic ratio $\beta = B/B_0$ = 0.659 and Dq/B = 0.796. From data obtained at T = 77 K that B = 636 cm^{-1}, C = 3404 cm^{-1} and $10Dq$ = 5025 cm^{-1}. Then nephelauxetic ratio $\beta = B/B_0$ = 0.662 and Dq/B = 0.790. Halenius [22] reported for genthelvite the following values: B = 663 cm^{-1}, C = 3408 cm^{-1}, $10Dq$ = 5350 cm^{-1}, so Dq/B = 0.807.

Table 8. The measured and calculated Mn^{2+}-bands genthelvite G1 sample.

Transitions/ Band Position (cm^{-1})	Halenius [22] T = 300 K	Current Study			
		Measured		Calculated	
		T = 300 K	T = 77 K	Equations (1) and (5) α = 0 cm^{-1} ε = 0.105	Equations (4) and (5) α = 65 cm^{-1} ε = 0.119
$^6A_1(^6S) \rightarrow {}^4T_1(^4G)$	20,930	21,520	?		
$^6A_1(^6S) \rightarrow {}^4T_2(^4G)$	22,570	22,750	22,530 (22,830 sh)		
$^6A_1(^6S) \rightarrow {}^4E,{}^4A_1(^4G)$	23,670	23,817	23,833	$^4A_1$: 23,471 ^4E: 23,944	23,104 23,030
$^6A_1(^6S) \rightarrow {}^4T_1(^4D)$	26,670	26,819	26,854 (26,553 sh)		
$^6A_1(^6S) \rightarrow {}^4E(^4D)$	28,310	28,248	28,286 (28,460 sh)	31,137	29,930
Spectroscopic parameters (cm^{-1})	*B* = 663 *C* = 3408 *Dq* = 535 *Dq*/*B* = 0.807	*B* = 633 *C* = 3497 *Dq* = 503.7 *Dq*/*B* = 0.796 Δ*E* = 0	*B* = 636 *C* = 3404 *Dq* = 502.5 *Dq*/*B* = *0.790* Δ*E* = *0*	*B* = 633 *C* = 3497 *Dq* = 503.7 *Dq*/*B* = 0.796 Δ*E* = 473	*B* = 756 *C* = 3324 *Dq* = 628 *Dq*/*B* = 0.83 Δ*E* = 74
Other parameters		β = 0.66	β = 0.66	β = 0.66 ε = 0.105 N_t^2 = 0.895	β = 0.78 ε = 0.119 N_τ^2 = 0.881

The genthelvite case can be used as a reference for willemite minerals studied here. The excitation bands are single, so there is no ambiguity in calculating the *B*, *C*, and *Dq* parameters. Consequently, *Dq*/*B* marked in Figure 13 as a solid yellow line may be a reference for calculated values of other minerals.

For genthelvite samples, no splitting of $^4E,^4A_1(^4G)$ was observed. The probable causes of $^4E^4A_1$ level splitting, or rather of its absence, are discussed below.

Firstly, only one site is predicated for Mn^{2+} in genthelvite structure, so there is no reason for the complex nature of the excitation spectrum. Second, the validity of the covalence theory was discussed. According to Equation (5), the calculated energies of $^4E^4A_1(^4G)$ levels are different from those actually observed. The calculations were made for two cases. In the first α = 0, so *B*, *C*, and *Dq* parameters were taken from experimental data, and the ε parameter was equal to 0.105. In the second, the α = 65 cm^{-1} was adopted, at which point *B*, *C*, and *Dq* had changed. In both cases, the Δ*E* parameter was not equal to zero. Let us note that the theoretical value of $^4A_1$ is greater than the value for ^4E, as expected by Curie et al. [12] only after introducing the Koide–Pryce α correction. Applying only ε parameter does not yield such results (Table 8). The calculated energy values of levels $^4A_1(^4G)$ and $^4E(^4G, {}^4D)$ are not close to the experimental data. Additionally, a different *Dq* value was calculated for the changed values of the *B* and *C* parameters. Consequently, the value of *Dq*/*B* = 0.83 is greater than that calculated from equation 2 (0.796). In that case, an emission band between 508 nm and 525 nm of willemite should be measured. These cases are marked in Figure 13 as yellow lines, solid and dotted, respectively. Therefore, this covalence theory approximation does not give results in sync with the experimental data for genthelvite. For this case, the difference in covalence of the orbitals t_2 and e is not quite the same as was predicated for LK = 4 [12]. Perhaps the reason is that the fourth ligand around Mn is sulfur, a ligand weaker than oxygen.

3.5.2. Willemite W2 Case

The calculation values of the spectroscopic parameters *B*, *C*, *Dq* for Mn^{2+} in the studied willemite W2 sample were presented in Table 9. The value of *B* and *C* Racah parameters must be computed from υ_5 and υ_3 transitions. First, it was checked whether the band at 23,121 cm^{-1} is not a component of υ_2 transition because in willemite, Mn^{2+} can occupy two non-equivalent lattice sites. The Racah parameter have been calculated for 23,710 cm^{-1} and 27,993 cm^{-1} band, so $B = 612$ cm^{-1}, $C = 3512$ cm^{-1}. From equation (2) for T1 MnO_4 tetrahedron and $\upsilon_2 = 22{,}770$ $cm^{-1,}$ it was calculated that $Dq = 512.8$ cm^{-1} and $Dq/B = 0.84$. If we assume that band at 23,133 cm^{-1} is the υ_2 band of a hypothetical T2 MnO_4 tetrahedron, then $Dq = 417$ cm^{-1}. Such a value of *Dq* is not controversial however, for this T2 site and value of $Dq/B = 0.68$, the emission line would have to be much shorter than the measured (525 nm), even shorter than for gethelvite (510 nm). It was estimated (Figure 13) that the emission should be a band at 480 nm, which was not confirmed by measurement. These two *Dq*/*B* values were indicated in Figure 13 by a green line, solid and dashed, respectively. For this reason, the band at 23,133 cm^{-1} cannot be considered as band υ_2 from the other, second lattice site. These calculations were shown earlier in Section 3.4.3. Previous calculations of *B* and *Dq* parameters were performed assuming that υ_3 line is a single band at 23,710 cm^{-1}. However, for room temperature measurements, the υ_3 band has two components: at 23,710 cm^{-1} and 23,133 cm^{-1}. Different ways of the *B* parameter calculating were considered. The available literature data so far does not provide a solution. Ten two cases were proposed:

(1) $E(^4A_1) > E(^4E)$ and we computed barycenter, so υ_3 now is equal 23,517 cm^{-1}
(2) $E(^4A_1) < E(^4E)$ and we computed barycenter, so υ_3 now is equal 23,325 cm^{-1}

Neither case (1) nor (2) gives results similar to the experimental ones (Table 9). For each of these cases, the *Dq*/*B* was too small to correspond to the emission at 525 nm. It can be noticed that it is even smaller than the *Dq*/*B* for genthelvite (0.800), which exhibits an emission band at 509 nm. Therefore, the simplest output should be assumed: for Tanabe–Sugano equations (1), the parameter *B* should be calculated for the highest component value of the υ_3 band.

For willemite W2 sample splitting of $^4E,^4A_1(^4G)$ $\Delta E = 577$ cm^{-1} and 660 cm^{-1} was observed at T = 300 K and T = 77 K, respectively. The probable causes of $^4E^4A_1(^4G)$ level splitting are discussed below.

The validity of covalence theory was discussed. According to equation (5) and for Koide–Pryce parameter $\alpha = 0$ cm^{-1}, the calculated energies of $^4E^4A_1(^4G)$ and $^4E(^4D)$ are greater than measured; the $^4A_1(^4G)$ lies below $^4E(^4G)$, contrary to covalence theory conclusions. Only ΔE calculated value is close to the observed. For $\alpha = 65$ cm^{-1}, $\varepsilon = 0.137$, ((I) in Table 9), the calculated energies of $^4E^4A_1(^4G)$ are now lower than measured, as a set of energy levels had now shifted to the opposite direction to the previous calculations. Contrary to covalence theory conclusions, the $^4A_1(^4G)$ lies below $^4E(^4G)$,. Unfortunately, ΔE calculated value is much smaller than the measured one. For α parameter less than 65 cm^{-1}, proposed $\alpha = 30$ cm^{-1}, $\varepsilon = 0.129$ ((II) in Table 9), the calculated energies of $^4E^4A_1(^4G)$ are lower than measured; the $^4A_1(^4G)$ lies below $^4E(^4G)$, contrary to covalence theory conclusions. Only ΔE calculated value is close to the observed. For other often used parameters $\alpha = 185$ cm^{-1}, $\varepsilon = 0.161$ ((III) in Table 9), the calculated energies of $^4E^4A_1(^4G)$ are now lower than for $\alpha = 65$ cm^{-1} and much lower than measured. The ΔE value looks better than for the previous calculation. However, the real root of the quadratic equation for the *Dq* value is possible only for $\alpha = 65$ cm^{-1} and $Dq = 728.4$ cm^{-1}, $Dq/B = 0.99$. The emission bands should be measured at about 560 nm.

These calculations made according to the covalence theory [12] show a split of the $^4E^4A_1(^4G)$ level, but the calculated values of energy of these levels differ significantly from the experimental data. Therefore, it can be concluded that this theory does not correctly describe the Mn^{2+} energy levels in willemite and does not explain the data obtained from the measurements.

Table 9. The measured and calculated Mn^{2+}-bands for willemite sample W2.

Transitions/Bands Position (cm^{-1})	Measured		Calculated				
				Equations (1) and (2)		Equation (5)	Equations (4) and (5) υ_3 = 23,710
	T = 300 K	T = 77 K	Equations (1) and (2)	(Case 1)	(Case 2)	α = 0 ε = 0.1025	(I) α = 65 (II) α = 30 (III) α = 185
$^6A_1(^6S) \rightarrow {}^4T_1(G)$	20,704–20,341	20,660–20,340	20,704–20,341				
$^6A_1(^6S) \rightarrow {}^4T_2(^4G)$	22,770	22,614	T1: 22,770 T2: 23,133	22,770	22,770		
$^6A_1(^6S) \rightarrow {}^4E,{}^4A_1(^4G)$	23,133 23,710	23,110 23,646 23,770	23,710	$^4A_1$: 23,710 ^4E: 23,133 (1) υ_3: 23,517	$^4A_1$: 23,133 ^4E: 23,710 (2) υ_3: 23,325	$^4A_1$: 23,537 ^4E: 24,094	$^4A_1$: (I): 22,632 (II): 22,842 (III): 22.003 ^4E: (I): 22,671 (II): 23,377 (III): 21,698
$^6A_1(^6S) \rightarrow {}^4T_1(^4D$	26,343 26,990	26,448	26,343 26,990	26,343 26,990	26,343 26,990		
Spectroscopic parameters (cm^{-1})	B = 612 C = 3518 Dq = 520.5 ΔE = 577	ΔE = 660	B = 612 C = 3518 Dq_1 = 520.5 Dq_1/B = 0.85 Dq_2 = 417 Dq_2/B = 0.68	B = 639.5 C = 3424 Dq = 472 Dq/B = 0.74	B = 666.8 C = 3331 Dq = 414.7 Dq/B = 0.62	B = 612 C = 3518 Dq_1 = 520.5 Dq_1/B = 0.85 ΔE = 557	(I): B = 735.4 C = 2410 (II): B = 669 C = 2500 (III): B = 957 C = 2097 ΔE = (I): 39 (II): 535 (III): 305

3.5.3. Willemite W1 Case

The calculation results of the B, C, Dq parameters for Mn^{2+} in the studied willemite sample are presented in Table 10.

Table 10. The measured and calculated Mn^{2+}-bands for willemite sample W1.

Transitions Band Positions (cm^{-1})	Halenius et al. [9]	This Work Measured		This Work Calculated		
				Equations (1) and (2)	Equation (5)	Equations (4) and (5)
		T = 300 K	T = 77 K		α = 0 ε = 0.103	α = 65 ε = 0.135
$^6A_1(^6S) \rightarrow {}^4T_1(^4G)$	T1: 20,370 T2: 21,230	20,462 20,811	20,462 20,794			
$^6A_1(^6S) \rightarrow {}^4T_2(^4G)$	T2: 22,700 T1: 23,120	22,820	22,771	T1: 22,771 T2: 23,287		
$^6A_1(^6S) \rightarrow {}^4E,{}^4A_1(^4G)$	T1 and T2: 23,700	23,279 23,877	23,272 23,809 23,935	23,775 23,935	$^4A_1$: 23,524 ^4E: 24,071	$^4A_1$: 22,684 ^4E: 22,746
$^6A_1(^6S) \rightarrow {}^4T_1(^4D)$	T2: 26,320 T1: 27,070	26,550 27,211	26,212 26,671 27,225			
$^6A_1(^6S) \rightarrow {}^4E(^4D)$	T1 and T2: 28,010	28,221	28.136 28,288	28,221	31,308	29,560
Other parameters	ΔE not identified	ΔE = 598	ΔE = 663	B = 620.5 C = 3534 Dq_1 = 562.8 Dq_1/B = 0.91 Dq_2 = 425.6 Dq_2/B = 0.68	ΔE = 547	B = 829.7 C = 2449 ΔE = 62

Using the previous discussion of calculations made for willemite W2, the bands at 28,221 cm^{-1} and 23,877 cm^{-1} were adopted for the *B* and *C* parameters calculations. Assuming the hypothesis about two Mn^{2+} lattice sites Halenius [9], two υ_2 bands should be selected. For T1 MnO_4 tetrahedron and υ_2 = 22,771 cm^{-1}, it was calculated that Dq = 562.8 cm^{-1}; Dq/B = 0.91. If we assume the 23,287 cm^{-1} as the υ_2 band of hypothetical T2 MnO_4 tetrahedron, then Dq = 425.6 cm^{-1} and Dq/B = 0.68. These cases were marked in Figure 13 as maroon lines, solid and dashed, respectively. Like the W2 case, the emission band should be measured at about 480 nm, which was not confirmed by measurement. For this reason, the band at 23,287 cm^{-1} cannot be considered as a band υ_2 corresponding to the other, second lattice site.

The calculated energy values of levels $^4A_1(^4G)$ and $^4E(^4G,^4D)$ with the covalent normalizing parameters did not bring results that are in line with the experimental data (just as was the case for the W2 sample). Moreover, similarly to that other sample, the modified values of B and C lead to the lack of a real root in the square equation of Dq. For this reason, we recognize that, as seen before for genthelvite and W2 sample, the correction for covalent bonding does not describe the obtained measurement results well.

It is worth noting that for many α values (Tables 9 and 10), the energy of the ^4E level is greater than $^4A_1$, unlike that shown by Curie et al. [12]. The willemite specimens studied here did not form automorphic crystals, so it was impossible to make polarized spectra that could decide about the energetic order of the ^4E and $^4A_1$ levels. The components of the υ_3 band on the spectra measured at T = 77 K for both W2 and W1 samples are separated in such a manner that the two higher energy bands lie closer to each other, and they probably belong to the ^4E sublevel. The third component, with the lowest energy, is perhaps the $^4A_1$ component. However, the lack of measurements in polarized light does not prove this.

4. Discussion

The probable causes of splitting of the $^4E^4A_1(^4G)$ level are discussed below. Data related to this effect were included in Table 11.

Table 11. The possible reasons for ΔE splitting.

Possible Reason	Number of Non-Equivalent Crystal Sites of Mn^{2+}	Site Symmetry	<MnO> (Å)	Geometrical Distortion				ΔE	
				Mean Quadratic Elongation (10^{-5})	Distortion Index	Quadra-Tic Elonga-Tion	Bond Angle Variance (deg^2)	Calculated Due Covalence (cm^{-1})	Measured (cm^{-1})
Genthelvite	one	C_3	2.0617	763 for O_3S 0 for O_3	0.06771	1.0279	50.2929	74	0
Willemite	two								
	Zn_1	C_1	1.9495	0.21	0.00130	1.0050	19.8536	W1: 62	W1: 598; 663
	Zn_2	C_1	1.9613	5.75	0.00704	1.0045	18.0387	W2: 39	W2: 577; 660

The values in the table are based on the reference willemite data [23].

(1) The Zn (Mn) site's geometric deformation indicators are higher for genthelvite than for willemite. However, the genthelvite excitation spectrum does not show $^4E^4A(^4G)$ splitting. This means that the real symmetry of the lattice site does not determine the ΔE value. For genthelvite, these geometric indicators have been calculated for O_3S, not for O_3 coordination. If we take after [21] that a coordination number of Zn is equal to 3.3608 and the effective coordination of Zn in genthelvite is O_3, then these geometric factors will become zero. On the other hand, when the sulphur atom as the fourth ligand is omitted, the Zn-O distance is shorter for genthelvite than for willemite, and by extension, Dq for genthelvite should be greater than for willemite, which is not actually the case. For willemite, the determined ΔE value is higher for the W1 sample than for sample W2. Manganese ions occupy the Zn_2 site in sample W2 and site Zn_1 in sample W1. The geometrical deformation parameters are greater for the Zn_2 site than for Zn_1. This is either the opposite of the expected effect or the absence of a relationship between deformation and cleavage. Sample W2 contains two times more manganese than sample W1. In turn, in

sample W2, only Mn^{2+} impurities were found, and in W1 an admixture of Mg^{2+}, exceeding the amount of Mn^{2+} was found. The significant difference of the Mg^{2+} and Mn^{2+} ion radii (0.57 and 0.66 Å, respectively) may cause a greater local deformation around Mn^{2+} in the structure of the W1 sample than for the W2 sample. In short, it can be said that the influence of the geometry of the coordination polyhedron on the value of ΔE is ambiguous.

(2) The calculations presented in Section 3.5 show that the theory of covalent bond participation does not give satisfactory results of the energies of the excited levels Mn^{2+}, nor the correct the values of the splitting of the $^4E^4A_1(^4G)$ level.

(3) The reason for the splitting may be the low symmetry of the position of Mn^{2+} in the crystal lattice: C_1 for willemite and C_3 for genthelvite. For spodumene $LiAlSi_2O_6$:Mn^{2+} and C_2 site symmetry ΔE = 414 cm^{-1} was observed [59]. However, the ΔE value for other minerals (talc, tremolite, poldervaarite, calcite, data in the study) with higher or lower local symmetry does not support this conclusion. However, incidentally, in calcite, where Mn^{2+} occupies a position with C_{3i} symmetry, the ΔE = 325 cm^{-1}.

(4) There was a significant difference in the ΔE value for willemite as measured by Palumbo and Brown [14] and equal 147 cm^{-1} and ΔE value about 600 cm^{-1} in the current study. There is some doubt that it was possible to measure by [14], side-by-side, lines differing by 0.4 nm, i.e., 420.4 nm (23,787 cm^{-1}) and 420.8 nm (23,764 cm^{-1}) since it was stated that the spectroscopic resolution was not better than 0.6 nm (page 1186, ibid.). In this study, no band at about 23,300 cm^{-1} was measured at all. Willemite studied by [14] contained four times less Mn. Despite the great interest in willemite as a photo-optical material, there is little data on the absorption or excitation bands for samples with different Mn content. All the data available so far has been discussed in the current paper.

The differences in the decay times for the G1 and G2 samples may be caused by different Mn content or by the presence of other lattice defects. Sample G2 contains two times less Mn^{2+} than sample G1. For G1, they are located approximately in every second, and for sample G2 in every third unit cell. The difference between the decay time for W1 and W2 samples is caused by the higher Mn-content in sample W2. The measured lifetimes of studied willemite samples are shorter than of genthelvite samples. There are three reasons for this effect. The first is the greater number of manganese atoms in the unit cell of studied W1 and W2 samples. For 36 Zn-atoms of the unit cell, there are 1.8 or 3.6 Mn atoms, respectively. The second reason is the smaller Zn-Zn distance in the willemite (3.112 Å) than in the genthelvite (~4 Å). The third is a lower symmetry of Mn-crystal site in willemite than in genthelvite. In the current study, the longest lifetimes (~3 and ~4 ms) have been measured for sample genthelvite G2. It is the sample with the lowest Mn content. As a similar value of lifetime was measured earlier for spodumene crystals containing up to 100 times less Mn [59], the higher site symmetry for genthelvite (C_3) than for spodumene (C_2), so the symmetry of crystal site is also an important factor.

For almost all synthetic α-Zn_2SiO_4 with different Mn^{2+} content, it has been shown that this ion occupies both lattice sites, usually preferring the larger Zn_2 site. The crystal field splitting parameter (Dq), as well as the Racah B parameter for Mn^{2+} derived for willemite samples W1 and W2, are not identical, and the difference in these values is significant. The comparison of the spectroscopic parameters is as follow:

sample W1 B = 620.5 cm^{-1}, β = 0.65, C = 3535 cm^{-1}, Dq = 562.8 cm^{-1}, Dq/B = 0.91,

sample W2 B = 612.0 cm^{-1}, β = 0.63, C = 3518 cm^{-1}, Dq = 520.5 cm^{-1}, Dq/B = 0.85.

The calculated crystal field parameter Dq is higher for W1 than for sample W2. It can be concluded that the Mn-O distance for the W1 sample is shorter than for sample W2. Based on these spectroscopic data, it was hypothesized that manganese ions occupy site Zn_1 in sample W1 and Zn_2 in sample W2. The longer the Mn-O bond, the smaller Dq is, and the bond is more covalent, also the Racah B parameter has a smaller value; this is the case for sample W2. Thus, a comparison of the spectroscopic results with Rietveld's structural data yields an elegant agreement. The energy of the $^4T_1(^4G)$ level from which the emission occurs depends not only on Dq but also on B, in terms of Tanabe–Sugano on

Dq/B, and these values are similar for samples W1 and W2. For this reason, no significant differences in the position of the emission band were observed for both samples.

5. Summary and Conclusions

The calculations of the spectroscopic parameters B, C, and Dq, as well as the energy of the excited levels, were made after some preliminary assumptions. There is no absolute certainty that they are correct in all cases.

First, we adopted the values of B and C that are the most commonly used in the literature on mineral spectroscopy. They were B = 960 cm^{-1} and C = 3325 cm^{-1} although B = 860 cm^{-1} is also used.

Second, there is no known method of determining the B parameter other than from the values of bands υ_3 and υ_5. The Mn^{2+} excitation or absorption spectra often show that the υ_3 band is no single but complex. In the current study, the υ_3 band component with the highest energy was selected for the calculation of B and C parameters. This was justified by the best fit of the Dq/B value on the Tanabe–Sugano diagram to the indisputable experimental value, i.e., the position of the emission band. However, the theoretical justification for this assumption is unknown.

Third, the electron Mn^{2+} transitions could couple with the lattice vibrations in a different way, maybe depending on the ion concentration or on the lattice site.

The discussion of the causes of the $^4E^4A_1(^4G)$ level split can be summarized as follows:

1. The performed calculations and their discussion led to the conclusion that the explanation of the cause of the $^4E^4A_1$ level split on the basis of the theory of the covalent bond participation does not give a result consistent with the measured data. The Koide–Pryce correction α and Curie et al. [2] formulas do not even produce good qualitative results for studied minerals.
2. The geometric deformation of the coordination polyhedron is not the factor determining the ΔE value.
3. Local site symmetry seems to be a quite important factor influencing the studied ΔE parameter. In the structure of willemite, the Mn^{2+} site symmetry is very low, C_s and C_1, while in genthelvite relatively high—C_3.
4. The presence, and perhaps the number of other point defects, apart from Mn, can be significant for willemite samples. This issue needs to be explored further.
5. The presented measured data, the results of the calculations, and the discussion mean that the ΔE value should be considered as an important spectroscopic parameter. So far, it is not known with what other parameters of the studied substances it is clearly and unequivocally related to. The greater number of experimental data obtained for samples with a different chemical composition and site symmetry of the manganese ion as well as the deformation of the coordination polyhedron should allow an assessment of the significance of the ΔE parameter and explain: (a) how to determine its value; and (b) what are the relevant factors at play. Some studies on calcite, talc, tremolite and poldervaartite are in preparation.

Author Contributions: Conceptualization, M.C.; Investigation/Measurements, M.C., R.L., R.J. and T.K.; Writing (Original Draft Preparation), M.C.; Writing (Review and Editing), M.C. and R.J.; Visualization, M.C., R.L. and R.J. All authors have read and agreed to the published version of the manuscript.

Funding: This research project was supported by the Working Group of Faculty of Natural Science, Institute of Earth Sciences, University of Silesia WNO/INoZ/2020_ZB02.

Data Availability Statement: Not applicable. The data is not publicly available, it is collected in the authors' scientific data collections and is the property of the University of Silesia.

Acknowledgments: The authors thank their colleague, PhD Eligiusz Szełęg, for taking photos of the genthelvite and willemite minerals, which are the subject of this manuscript.

Conflicts of Interest: The authors declare no conflict of interest.

References

1. Zhou, Q.; Dolgov, L.; Srivastava, A.M.; Zhou, L.; Wang, Z.; Shi, J.; Dramićanin, M.D.; Brik, M.G.; Wu, M. Mn^{2+} and Mn^{4+} Red Phosphors: Synthesis, Luminescence and Applications in WLEDs. A Review. *J. Mater. Chem. C* **2018**, *6*, 2652–2671. [CrossRef]
2. Rouz'e l'Alzit, F.; Bazin, T.; Poulon-Quintin, A.; Champion, E.; Bertrand, C.; Cardinal, T.; Rougier, A.; Mherji, I.; Jubera, V.; Gaudon, M. Thermochromoluminescence Mn^{2+}-Doped oxides as thermal sensor for selective laser sintering. *Opt. Mater.* **2020**, *110*, 110542. [CrossRef]
3. Wang, J.; Lou, S.; Li, P. Enhanced orange-red emission of $Sr_3La(PO_4)_3$:Ce^{3+}, Mn^{2+} via energy transfer. *J. Lumin.* **2014**, *156*, 87–90. [CrossRef]
4. Lei, B.; Liu, Y.; Ye, Z.; Shi, C. Luminescence properties of $CdSiO_3$:Mn^{2+} phosphor. *J. Lumin.* **2004**, *109*, 215–219. [CrossRef]
5. Gong, Y.; Wang, Y.; Xu, X.; Li, Y.; Xin, S.; Shi, L. The persistent energy transfer of Eu^{2+} and Mn^{2+} and the thermoluminescence properties of long-lasting phosphor $Sr_3MgSi_2O_8$:Eu^{2+}, Mn^{2+}, Dy^{3+}. *Opt. Mater.* **2011**, *33*, 1781–1785. [CrossRef]
6. Burns, R.G. *Mineralogical Applications of Crystal Field Theory*, 2nd ed.; Cambridge University Press: New York, NY, USA, 1993.
7. Marfunin, A.S. *Physics of Minerals and Inorganic Materials. An Introduction*; Springer: Berlin/Heidelberg, Germany, 1979; 342p.
8. Wortman, D.E.; Morrison, C.A. Analysis of the energy levels of Mn^{2+} in halo apatite structures. *Opt. Mater.* **1995**, *4*, 487–505. [CrossRef]
9. Halenius, U.; Bosi, F.; Skogby, H. Galaxite, $MnAl_2O_4$, a spectroscopic standard for tetrahedrally coordinated Mn^{2+} in oxygen-based mineral structures. *Am. Miner.* **2007**, *92*, 1225–1231. [CrossRef]
10. Robinson, K.; Gibbs, G.V.; Ribbe, P.H. Quadratic elongation: A quantitative measure of distortion in coordination polyhedra. *Science* **1971**, *172*, 567–570. [CrossRef] [PubMed]
11. Fleet, M. Distortion parameters for coordination polyhedra. *Mineral. Mag.* **1976**, *40*, 531–533. [CrossRef]
12. Curie, D.; Batrhou, C.; Canny, B. Covalent bonding of Mn^{2+} ions in octahedral and tetrahedral coordination. *J. Chem. Phys.* **1974**, *61*, 3048–3062. [CrossRef]
13. Stout, J.W. Absorption Spectrum of Manganous Fluoride. *J. Chem. Phys.* **1959**, *31*, 709–719. [CrossRef]
14. Palumbo, D.T.; Brown, J.J., Jr. Electronic States of Mn^{2+}-Activated Phosphors: I. Green-Emitting Phosphors. *J. Electrochem. Soc.* **1970**, *117*, 1184–1188. [CrossRef]
15. Powell, R.C. *Properties of Solid-State Laser Materials*; AIP, Springer: New York, NY, USA, 1988.
16. Chang, Y.M.; Rudowicz, C.; Yeung, Y.Y. Crystal filed analysis of the $3d^N$ ions at low symmetry sites including the "imaginary" terms. *Comput. Phys.* **1994**, *8*, 583–588. [CrossRef]
17. Brik, M.G.; Teng, H.; Lin, H.; Zhou, S.; Avram, N.M. Spectroscopic and crystal field studies of $LiAlO_2$:Mn^{2+} single crystals. *J. Alloys Compd.* **2010**, *506*, 4–9. [CrossRef]
18. Vaida, M. Energy Levels and Effective Spin-Hamiltonian Parameters for Mn^{2+} Ions in Zn_2SiO_4. *AIP Conf. Proc.* **2012**, *1472*, 204–209.
19. Vaida, M. Crystal field parameters and low-lying energy levels for Mn^{2+} doped in Zn_2SiO_4. *Optoelectron. Adv. Mater. Rapid. Commun.* **2012**, *6*, 713–716.
20. Su, F.; Ma, B.; Ding, K.; Li, G.; Wang, S.; Chen, W.; Joly, A.G.; McCready, D.E. Luminescence temperature and pressure studies of Zn_2SiO_4 phosphors doped with Mn^{2+} and Eu^{3+} ions. *J. Lumin.* **2006**, *116*, 117–126. [CrossRef]
21. Hassan, I.; Grundy, H.D. The crystal structures of helvite group minerals, $(Mn,Fe,Zn)_8(Be_6Si_6O_{24})S_2$. *Am. Mineral.* **1985**, *70*, 186–192.
22. Halenius, U. Absorption of light by exchange coupled pairs of tetrahedrally coordinated divalent manganese in the helvite-genthelvite solid solution. *Period. Mineral.* **2011**, *80*, 105–111.
23. Klaska, K.-H.; Eck, J.C.; Pohl, D. New Investigation of Willemite. *Acta Cryst.* **1978**, *B34*, 3324–3325. [CrossRef]
24. Kim, Y.-I.; Im, W.B.; Ryu, K.-S.; Kim, K.-B.; Lee, Y.-H.; Lee, J.S. Combined Rietveld refinement of Zn_2SiO_4:Mn^{2+} using X-ray and neutron powder diffraction data. *Nucl. Instrum. Meth. B* **2010**, *268*, 346–351. [CrossRef]
25. Behal, D.; Röska, B.; Gattermann, U.; Reul, A.; Park, S.-H. Structure analysis of a Mn-doped willemite-type compound, $(H_{0.12}Zn_{1.89(3)}Mn_{0.05(1)}\square_{0.06})Si_{1.00(1)}O_4$. *J. Solid State Chem.* **2014**, *210*, 144–149. [CrossRef]
26. Dunn, P.J. Genthelvite and the helvine group. *Mineral. Mag.* **1976**, *40*, 627–636. [CrossRef]
27. Finch, A.A. Genthelvite and Willemite, Zinc Minerals Associated with Alkaline Magmatism from the Motzfeld Centre, South Greenland. *Mineral. Mag.* **1990**, *54*, 407–412. [CrossRef]
28. Antao, S.M.; Hassan, I. A two-phase intergrowth in genthelvite from Mont Saint Hilaire, Quebeck. *Can. Mineral.* **2010**, *48*, 1217–1223. [CrossRef]
29. Gaines, R.V.; Skinner, H.C.W.; Foord, E.E.; Mason, B.; Rosenzweig, A. *Dana's New Mineralogy. The System of Mineralogy of James Dwight Dana and Edward Salisbury Dana*, 8th ed.; Wiley-Interscience: Hoboken, NJ, USA, 1997; ISBN 978-0471193104.
30. Metcalf-Johansen, J. Willemite from the Ilímaussaq alkaline Intrusion. *Mineral. Mag.* **1977**, *41*, 71–75. [CrossRef]
31. Simonov, M.A.; Sandomirskii, P.A.; Egorov-Tismenko, Y.K.; Belov, N.V. Crystal structure of willemite, $Zn_2[SiO_4]$. *Dokl. Akad. Nauk SSSR+* **1977**, *237*, 581–584.
32. Sreekanth Chakradhar, R.P.; Nagabhushana, B.M.; Chandrappa, G.T.; Ramesh, K.P.; Rao, R.L. Solution combustion derived nanocrystalline Zn_2SiO_4: Mn phosphors: An spectroscopic view. *J. Chem. Phys.* **2004**, *121*, 10250–20259. [CrossRef] [PubMed]
33. Perkins, H.K.; Sienko, M.J. ESR Study of Manganese-Doped α-Zinc Silicate Crystals. *J. Chem. Phys.* **1967**, *46*, 2398–2401. [CrossRef]

34. Stevels, A.L.N.; Vink, A.T. Fine structure in the low temperature luminescence of Zn_2SiO_4:Mn and $Mg_4Ta_2O_9$:Mn. *J. Lumin.* **1974**, *8*, 443–451. [CrossRef]
35. Hang, C.; Simonov, M.A.; Belov, N.V. Crystal structures of willemite $Zn_2[SiO_4]$ and its germanium analog $Zn_2[GeO_4]$. *Sov. Phys. Crystallogr.* **1970**, *15*, 387–390.
36. Mofrad, A.M.; Peixoto, C.; Blumeyer, J.; Liu, J.; Hunt, H.K.; Hammond, K.D. Vibrational Spectroscopy of Sodalite: Theory and Experiments. *J. Phys. Chem. C* **2018**, *122*, 24765–24779. [CrossRef]
37. Rudolf, W.W.; Fischer, D.; Irmer, G.; Pye, C.C. Hydration of beryllium(II) in aqueous solutions of common inorganic salts. A combined vibrational spectroscopic and *ab initio* molecular orbital study. *Dalton Trans.* **2009**, *23*, 6513–6521. [CrossRef] [PubMed]
38. Rudolf, W.W. Raman and Infrared Spectroscopic Investigation of Speciation in $BeSO_4$(aq). *J. Solut. Chem.* **2009**, *39*, 1039–1058. [CrossRef]
39. Chandra Babu, B.; Buddhudu, S. Analysis of structural and electrical properties of Ni^{2+}: Zn_2SiO_4 ceramic powders by sol–gel method. *J. Sol-Gel. Sci. Technol.* **2014**, *70*, 405–415. [CrossRef]
40. Syamimi, N.F.; Matori, K.A.; Lim, W.F.; Aziz, S.A.; Zaid, M.H.M. Effect of Sintering Temperature on Structural and Morphological Properties of Europium (III) Oxide Doped Willemite. *J. Spectrosc.* **2014**, *2014*, 328931. [CrossRef]
41. Sarrigani, G.V.; Quah, H.J.; Lim, W.F.; Matori, K.A.; Moh Razali, N.S.; Kharazmi, A.; Hashim, M.; Bahari, H.R. Characterization of Waste Material Derived Willemite-Based Glass-Ceramics Doped with Erbium. *Adv. Mat. Sci. Eng.* **2015**, *2015*, 953659. [CrossRef]
42. Chandra Babu, B.; Vengla Rao, B.; Ravi, M.; Babu, S. Structural, microstructural, optical, and dielectric properties of Mn^{2+}: Willemite Zn_2SiO_4 nanocomposites obtained by a sol-gel method. *J. Mol. Struct.* **2017**, *1127*, 6–14. [CrossRef]
43. Chandra Babu, B.; Wanga, G.-G.; Yana, B.; Yanga, Q.; Baker, A.P. Effects of Cr^{3+} addition on the structure and optical properties of α-Zn_2SiO_4 synthesized by sol-gel method. *Ceram. Int.* **2017**, *44*, 938–946. [CrossRef]
44. Alibe, I.M.; Matori, K.A.; Sidek, H.A.A.; Yaakob, Y.; Rashid, U.; Alibe, A.M.; Zaid, M.H.M.; Khiri, M.Z.A. Effects of Calcination Holding Time on Properties of Wide Band Gap Willemite Semiconductor Nanoparticles by the Polymer Thermal Treatment Method. *Molecules* **2018**, *23*, 873. [CrossRef]
45. Dimitrov, T.I.; Markovska, I.G.; Ibreva, T.H. The Analysis about Synthesis, Structure and Properties of Willemite Ceramic Pigments Obtained by a Sol–Gel Method. *Mater. Sci. Eng.* **2020**, *893*, 012001. [CrossRef]
46. Bursthein, Z.; Henderson, D.O.; Morgan, S.; Silberman, E. Vibrational spectra of chrysoberyl. *J. Phys. Chem. Solids* **1989**, *50*, 1095–1100. [CrossRef]
47. Jehlička, J.; Vandenabeele, P.; Edwards, H.G.M. Discrimination of zeolites and beryllium containing silicates using portable Raman spectroscometric equipment with near-infrared excitation. *Spectrochim. Acta A* **2012**, *86*, 341–346. [CrossRef] [PubMed]
48. Handke, M.; Urban, M. IR and Raman spectra of alkaline earth metals orthosilicates. *J. Mol. Struct.* **1982**, *79*, 353–356. [CrossRef]
49. McMillan, P. Structural studies of silicate glasses and melts applications and limitations of Raman spectroscopy. *Am. Mineral.* **1984**, *69*, 622–644.
50. Chopelas, A. Single crystal Raman spectra of forsterite, fayalite, and monticellite. *Am. Mineral.* **1991**, *76*, 1101–1109.
51. Dalby, K.N.; King, P.L. A new approach to determine and quantify structural units in silicate glasses using micro-reflectance Fourier-Transform infrared spectroscopy. *Am. Mineral.* **2015**, *91*, 1783–1793. [CrossRef]
52. Essalaha, G.; Kadimb, G.; Jabarb, A.; Masrourb, R.; Ellouzea, M.; Guermazia, H.; Guermazi, S. Structural, optical, photoluminescence properties and Ab initio calculations of new Zn_2SiO_4/ZnO composite for white light emitting diodes. *Ceram. Int.* **2020**, *46*, 12656–12664. [CrossRef]
53. Griffith, W.P. Raman studies on rock-forming minerals. Part I. Orthosilicates and cyclosilicates. *J. Chem. Soc. A* **1969**, 1372–1377. [CrossRef]
54. Gorobets, B.; Rogojine, A. *Luminescence Spectra of Minerals. Handbook*; RCP VIMS: Moscow, Russia, 2001.
55. Bertail, C.; Maronm, S.; Buisette, V.; Le Mercier, T.; Gacoin, T.; Boilot, J.-P. Structural and Photoluminescence Properties of Zn_2SiO_4:Mn^{2+} Nanoparticles Prepared by a Protected Annealing Process. *Chem. Mater.* **2011**, *23*, 2961–2967. [CrossRef]
56. Rivera-Enríquez, C.E.; Fernández-Osorio, A.; Chávez-Fernández, J. Luminescence properties of α- and β-Zn_2SiO_4:Mn nanoparticles prepared by a coprecipitation method. *J. Alloys Compd.* **2016**, *688*, 775–782. [CrossRef]
57. Kretov, M.A.; Iskandranova, I.M.; Potapkin, B.V.; Scherbinin, A.V.; Srivastava, A.M.; Stepanov, N.F. Simulation of structured $^4T_1 \rightarrow {}^6A_1$ emission bands of Mn^{2+} impurity in Zn_2SiO_4: A first principal methodology. *J. Lumin.* **2012**, *132*, 2143–2150. [CrossRef]
58. Hu, T.; Xu, J.; Wang, B.; Wang, J.; Wang, Y. Color-Tunable Persistent Luminescence in Oxyfluoride Glass and Glass Ceramic Containing Mn^{2+} :α-Zn_2SiO_4 Nanocrystals. *J. Mater. Chem. C* **2017**, *5*, 1479–1487. [CrossRef]
59. Czaja, M.; Lisiecki, R.; Kądziołka-Gaweł, M.; Winiarski, A. Some Complementary Data about the Spectroscopic Properties of Manganese Ions in Spodumene Crystals. *Minerals* **2020**, *10*, 554. [CrossRef]